Influence of an inertia-gravity wave on mesospheric dynamics: A case study with the Poker Flat Incoherent Scatter Radar

M. J. Nicolls,[1] R. H. Varney,[2] S. L. Vadas,[3] P. A. Stamus,[3] C. J. Heinselman,[1] R. B. Cosgrove,[1] and M. C. Kelley[2]

Received 10 February 2010; revised 7 June 2010; accepted 15 June 2010; published 7 October 2010.

[1] A case study of mesospheric winds and waves observed by the Poker Flat Incoherent Scatter Radar (PFISR) on 23 April 2008 is presented. Active auroral precipitation created sufficient ionization for nearly 12 h of continuous incoherent scatter measurements of the *D* region ionosphere from ~60 to 90 km altitude. PFISR utilized a multilook-direction mode which permitted measurements of vector winds, in addition to high precision vertical velocities, at high temporal resolution. A large-amplitude coherent wave packet (appearing superficially to be a single wave) with a downward phase velocity and a long period ($\tau \sim 10.5$ h) was observed. Vertical wavelengths were measured directly to be $\lambda_z \simeq 4$–10 km, increasing with altitude. The proximity of τ to the local inertial period in addition to its large horizontal wavelength are suggestive of a coherent inertia-gravity wave (IGW) packet. Using polarization analyses, we find that the IGWs are propagating mainly southward. The waves were observed to saturate at $z \sim 70$–85 km, and have their largest amplitudes in the first 8 h of the measurements (before 2000 UT). A stability analysis confirms that the waves were likely dynamically unstable at these altitudes and times. In conjunction with this observation, the background wind is found to be southward of HWM winds by 10–20 m/s until ~2000 UT, consistent with the horizontal background wind acceleration created by the saturation of these IGWs. After 2000 UT, the background wind relaxes to the north by 10–20 m/s, consistent with a significant decrease of the IGW amplitudes. The IGWs may have originated from a jet stream adjustment at $z \sim 10$ km in northern Russia about 5 days prior to the observation in Alaska.

Citation: Nicolls, M. J., R. H. Varney, S. L. Vadas, P. A. Stamus, C. J. Heinselman, R. B. Cosgrove, and M. C. Kelley (2010), Influence of an inertia-gravity wave on mesospheric dynamics: A case study with the Poker Flat Incoherent Scatter Radar, *J. Geophys. Res.*, *115*, D00N02, doi:10.1029/2010JD014042.

1. Introduction

[2] Gravity waves are an important component of the upper atmospheric environment, wherein they transport energy and momentum, generate turbulence, and interact with the mean flow (e.g., see reviews by *Fritts* [1984] and *Fritts and Alexander* [2003]). Inertia-gravity waves (IGWs) are low-frequency waves that are influenced by the rotation of the Earth, often observed in the troposphere and stratosphere using balloon-borne radiosondes [e.g., *Cot and Barat*, 1986; *Barat and Cot*, 1992; *Tsuda et al.*, 1994; *Vincent and Alexander*, 2000; *Guest et al.*, 2000] and mesosphere-stratosphere-troposphere (MST) radars [e.g., *Cornish and Larsen*, 1989; *Thomas et al.*, 1992; *Sato*, 1994; *Mitchell et al.*, 1994; *Cho*, 1995; *Riggin et al.*, 1995, 1997; *Serafimovich et al.*, 2005; *Nastrom and Eaton*, 2006]. IGWs in the mesosphere and lower thermosphere have been occasionally studied with MST radars and lidars [e.g., *Muraoka et al.*, 1987; *Murakoa et al.*, 1988; *Gavrilov et al.*, 1996; *Hu et al.*, 2002; *Williams et al.*, 2004; *Li et al.*, 2007]; however, these are much more rare than lower-altitude observations, since the waves tend to be filtered out by the background winds as they propagate upward as a result of their very low vertical phase speeds [e.g., *Fritts and Alexander*, 2003]. Thus IGWs tend to be of secondary importance for upper atmospheric coupling processes, whereas convectively generated waves in the spring, summer, and fall and hemispheric mountain waves in the winter are thought to be of primary importance. Smaller-scale waves tend to have higher energy fluxes for a given energy density [e.g., *Fritts and VanZandt* 1993] and observations show that the majority of mesospheric momentum flux is due to short-period ($\tau < 1$ h) waves [e.g., *Fritts and Vincent* 1987].

[3] Nevertheless, there are many observations at polar latitudes of near-inertial frequency oscillations [e.g., *Hernandez et al.*, 1992; *Collins et al.*, 1992; *Collins and Smith*, 2004].

[1]Center for Geospace Studies, SRI International, Menlo Park, California, USA.
[2]School of Electrical and Computer Engineering, Cornell University, Ithaca, New York, USA.
[3]CoRA Division, Northwest Research Associates, Boulder, Colorado, USA.

0148-0227/10/2010JD014042

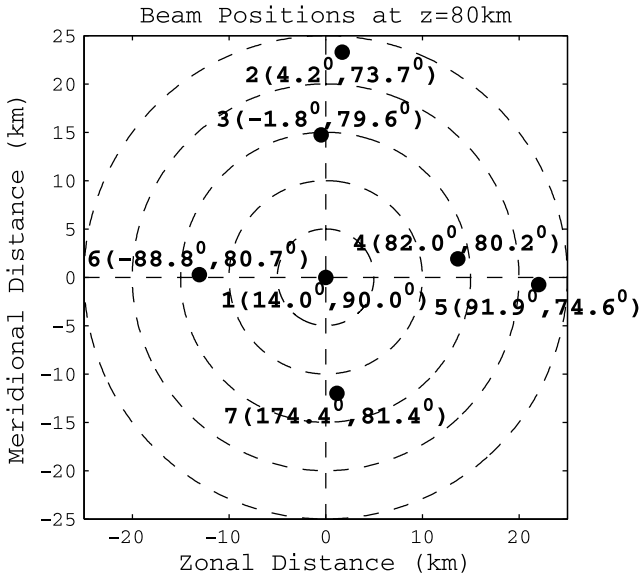

Figure 1. Location of the seven beams at 80 km altitude. The azimuth (east of north) and elevation angles for each beam are indicated. The dashed circles correspond to radial distances plotted every 5 km.

At high latitudes, the inertial frequency is close to the frequency of the semidiurnal tide. Thus it is thought that inertia-gravity waves play a role in the day-to-day variability of the semidiurnal tide observed at mesospheric altitudes via mean-flow interactions [e.g., *Walterscheid*, 1981], effectively generating a "pseudo-tide" [*Walterscheid et al.*, 1986]. Direct observations of gravity wave accelerations of the mean flow are rare.

[4] The generation of IGWs is associated with jet streams in the troposphere, and the waves tend to be radiated from regions of significant geostrophic adjustment (restoration of balanced flow) [e.g., *Fritts and Alexander*, 2003]. Details of the forcing mechanisms that generate the IGWs have been elucidated by modeling studies [e.g., *Zhu and Holton*, 1987; *Fritts and Luo*, 1992; *Luo and Fritts*, 1993; *Vadas and Fritts*, 2001; *Vadas et al.*, 2003], which have shown that gravity wave responses to a local horizontal body force depend both on the spatial characteristics of the forcing function as well as the duration of the forcing [*Vadas and Fritts*, 2001; *Vadas et al.*, 2003]. The body forcing tends to generate waves with significant amplitudes at periods slightly less than and longer than the force duration, with vertical wavelengths peaking at ~1–2 times the vertical extent of the force, and with horizontal wavelengths peaking at ~2 times the horizontal extent of the force [*Vadas et al.*, 2003]. These waves propagate vertically and grow nearly exponentially with altitude [*Hines*, 1960], until they reach a critical level or saturate/dissipate. At this altitude, they deposit at least some of their momentum and energy into the background flow.

[5] In this paper we present a study of an observed IGW using measurements made with the Poker Flat Incoherent Scatter Radar (PFISR), which is the initial deployment of the Advanced Modular Incoherent Scatter Radar (AMISR) class of ISRs. PFISR's pulse-to-pulse beam steering capability has previously been used to investigate the dynamics of *F* region gravity waves, allowing for the determination of the propagation directions, periods, and horizontal wavelengths of GWs [*Nicolls and Heinselman*, 2007; *Vadas and Nicolls*, 2008, 2009]. This study uses incoherent scatter from the *D*-region ionosphere as a tracer of the neutral dynamics in the 70–90 km region. This portion of the ionosphere is collisionally dominated, so the plasma motions are indicative of the neutral motions.

2. Experiment and Methodology

[6] PFISR is located at the Poker Flat Research Range (65.13°N, 147.47°W) near Fairbanks, Alaska. PFISR has the ability to steer on a pulse-to-pulse basis, providing a powerful extension over typical ISRs. The radar is tilted so that its boresight direction corresponds to elevation and azimuth angles of 74° and 15°, respectively. The beamwidth of PFISR is approximately 1°–1.5°, with the larger dimension in the plane perpendicular and north to the radar face, and the peak power for this experiment was approximately 1.7 MW. For further system details, see *Nicolls et al.* [2007] and *Heinselman and Nicolls* [2008].

[7] The experimental configuration used for *D*-region experiments with PFISR has varied based on experimental goals. The beam configuration used for the experiment on 23 April 2008 is shown in Figure 1, where the *x*-*y* positions of the different beams relative to the radar are shown at 80 km altitude. This configuration uses seven beams pointed at a range of azimuth and elevation angles (including a vertical beam) so as to make the problem of determining winds and other parameters (such as momentum fluxes) overdetermined. This is often necessary as ionization mechanisms in the high-latitude *D* region, namely energetic particle precipitation, can be sporadic and have large spatial and temporal gradients.

[8] The experiment consisted of binary phase-coded transmissions designed to utilize the full duty cycle of the system, which is close to 10%. The mode is similar to that described by *Janches et al.* [2009] in the original *D* region measurements and by *Nicolls et al.* [2009] for polar mesospheric summer echo (PMSE) measurements. The mode consisted of transmitting a 280-μs, 28-baud binary-phase coded pulse with 10 μs (1.5 km) bauds sampled at 5 μs. Other experiments [e.g., *Janches et al.*, 2009; *Nicolls et al.*, 2009] have used Barker-coded pulses and/or shorter baud lengths (limited by a bandwidth allocation to 4 μs) to increase range resolution. Duty cycle limitations for this experiment resulted in a choice of interpulse period (IPP) of 3 ms, leading to self clutter at range intervals of 450 km.

[9] Typically, 128 pulses are transmitted in each direction before switching the look direction, and pulse-to-pulse autocorrelation functions (ACFs) are computed, from which power spectral estimates are deduced. Seven full cycles (ideally 896 pulses in all directions) are typically completed before writing raw data to disk. These experimental parameters allow for a highest frequency resolution of 1.3 Hz and a Nyquist frequency of 167 Hz, which limits the upper altitude of useful measurements as the spectra broaden due to decreasing ion-neutral collisions. These parameters also determine the highest spectral time resolution of 2.7 s at the full Doppler resolution (although the time resolution can be improved if frequency resolution is sacrificed). A simple clutter removal scheme was employed that involved the subtraction of the DC component of the raw voltages,

estimated as a median of the complex voltages over the full 896-pulse sequence for each look direction. In addition, an outlier removal scheme was applied to the raw complex voltages over the full 896-pulse sequence before computing power and autocorrelation function estimates. This method is described in Appendix A.

[10] For the purposes of direct power estimates from the voltage measurements, noise estimates were obtained from ranges below those of interest but above contaminating ground and tropospheric clutter sources, from 55 to 65 km. Received power was calibrated to absolute volume reflectivity using injected calibration pulses from another experiment and a system constant approach as described by *Nicolls et al.* [2007], based on long-term plasma line calibrations to the *F* region peak electron density.

[11] For this experiment, ACF estimates were formed by summing over seven full cycles, corresponding to a time of ~19 s. The spectra were combined with an outlier elimination algorithm (similar to that described in Appendix A) over an additional 10–30 groups (overall integration time of ~3–10 min). Spectra were fit for a turbulence-broadened incoherent scatter spectrum, which is known as a Voigt function and described in Appendix B. Spectra were fit for both a turbulent (Gaussian) and incoherent scatter (Lorentzian) component, as described in Appendix B. Examples of spectra and spectral fits to 10-min integrated measurements from three representative beams directed to the vertical, north, and east are shown in Figure 2. The spectra are roughly Lorentzian in shape with increasing spectral width and amplitude as a function of altitude [e.g., *Dougherty and Farley*, 1963; *Mathews*, 1978, 1986]. Spectral widths above ~90 km are too wide to be resolved using these measurements. Spectra in the vertical direction show nearly no Doppler motion as expected. Horizontal motion is evident in the north and east beams with a clear wave-like signature in the Doppler velocities. The amplitude of the spectral fits can also be used to give a very precise measure of electron density, which is described in the next section.

3. Observations

3.1. Electron Densities

[12] The observations presented in this paper were made possible by reasonable (and unusual) signal strengths detected from the 60–90 km altitude range. The high electron densities needed for such observations were afforded by hard auroral particle precipitation, similar to the conditions reported by *Janches et al.* [2009]. In this paper, we assume that the conditions that made these observations possible did not affect the dynamics of the region or the generality of our conclusions. While this is likely a good assumption, there is some evidence that this region can in some situations be affected by geomagnetic activity via Joule heating and other mechanisms [e.g., *Johnson and Luhmann*, 1993]. The median electron densities combined from all beams and binned in 5-km altitude intervals, are shown in Figure 3 as a function of time from 0000 to 2400 UT. The median N_e over the period 1200–2400 UT is also shown (solid line), along with the median from 0000 to 0200 UT (dashed line) where no enhanced ionization was observed. Note that at these low values of N_e, the measurements are at their sensitivity limitations and highly error-prone. Periods of enhanced electron density occurred between 1600–1800 UT and 2100–2300 UT, but electron densities were sufficiently high over the entire 12 h period from 1200 to 2400 UT to measure spectra and derive parameters from 60 to nearly 90 km in altitude (limited at the upper altitudes by the broadening spectra). These electron densities were computed from the amplitude of the Lorentzian fits described in section 2. Spectra could also be measured between 0300 and 0500 UT to very low altitudes and from 0700 to 1100 UT at altitudes above 75 km. Electron densities reached as low as 2×10^9 m^{-3} at the lower altitudes (~60 km); however, spectra at these ranges were still able to be resolved because of the narrow spectral widths. For PFISR's ~450 MHz operating frequency, the Debye limit ($4\pi\lambda_D^2/\lambda_R^2 \approx 1$) is not encountered until densities less than $\sim 5 \times 10^8$ m^{-3} for reasonable mesospheric temperatures. This, combined with the high spectral resolution afforded by these measurements, allows for routine observations of the *D* region to low altitudes. One of the main limitations leading to the lower altitude bound of such measurements is ground clutter, which, depending on the pulse sequence used, extends to ranges of 55–60 km for PFISR.

3.2. Radial Velocities

[13] Radial velocities were determined by the procedure described in section 2, wherein an analytical curve (see Appendix B) was fit to the Doppler spectra. For 10-min integrations during the periods of highest ionization (1600–1800 UT and 2100–2300 UT) errors on radial velocities below 75–80 km were less than 0.1 m/s. For the period 1800–2000 UT, where moderate densities were observed, errors were less than 0.5 m/s, increasing to ~1 m/s above 80 km. For the period 12–16 UT, errors were still quite small, ~1 m/s. Shorter time integrations were also investigated and these were also extremely robust (as short as 2 min integrations were used); however, such resolution is not needed for this study.

[14] The radial velocities for the full 24-h period are shown in Figure 4 from each beam independently. Periods where sufficient ionization was present to illuminate the mesospheric region are marked by the presence of very clear wave activity. The radial velocities represent the projection of the winds onto the look directions. The vertical speeds are extremely small, whereas the velocities in the off-vertical-looking beams reach up to 15 m/s, implying significant horizontal motion. As can be seen in Figure 1, beams 2, 3, and 7 nearly lie along a north-south (geographic meridional) line, and beam 4, 5, and 6 nearly lie along an east-west (zonal) line. The radial scale in Figure 1 corresponds to the separation between the beams in kilometers at an altitude of 80 km. The anticorrelation between beam 7 (directed toward the south) and beams 2 and 3 (directed toward the north), as well as beam 6 (directed toward the west) and beams 4 and 5 (directed toward the east) is evident, which implies uniform horizontal motion. A correlation analysis (not shown) confirms this result.

3.3. Winds

[15] Radial velocity measurements presented in Figure 4 imply that the horizontal wavelength of the wave must be much larger than the horizontal separation between the beams, as no phase differences are observed between the different look directions. The high degree of correlation

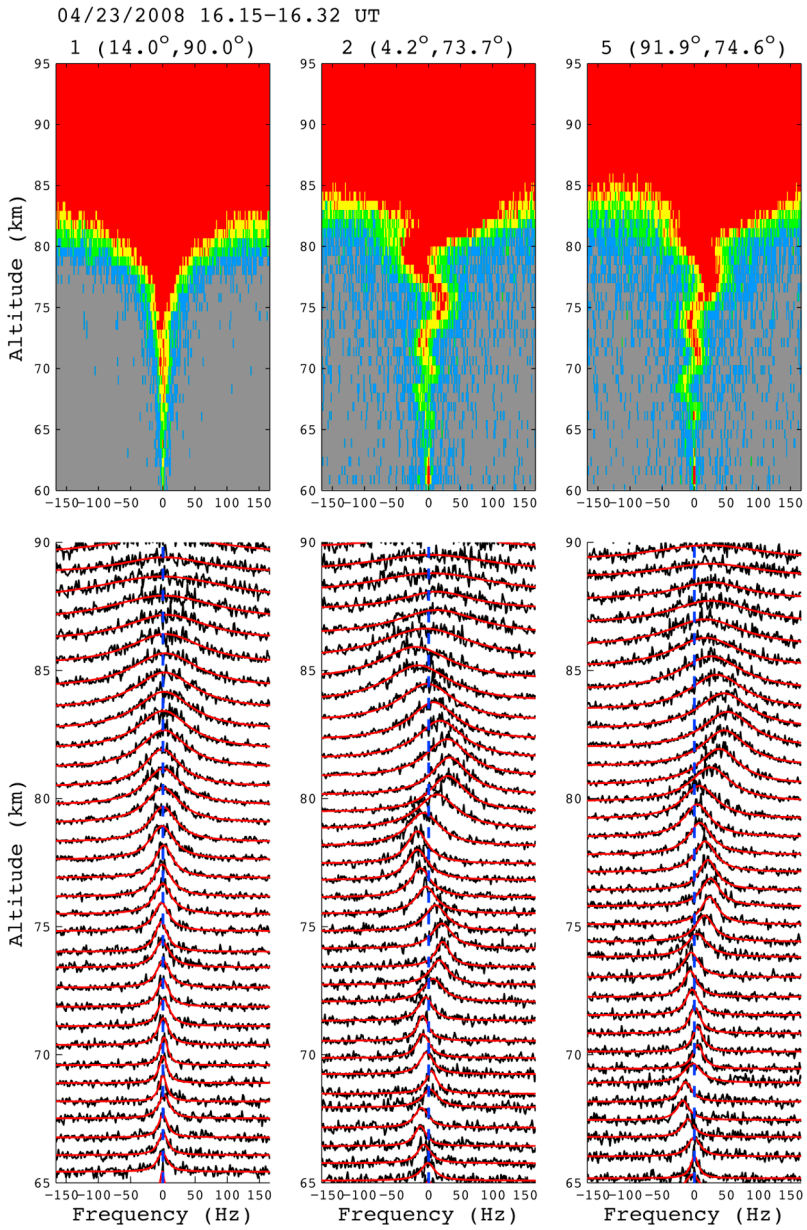

Figure 2. (top) Examples of 10-min integrated spectra obtained on 23 April 2008 near 1600 UT on a log scale from three representative beams directed toward the vertical (1), the north (2), and the east (3). (bottom) Line spectra (black) and fits (red) at every second range gate from 65 to 90 km for the same three beams.

between the beams permits the assumption that the winds are uniform over the field-of-view of the radar (which is at most 30 km at 80 km altitude). The radial velocities measured by each beam correspond to the projection of the vector wind field onto the line-of-sight, i.e.,

$$\begin{pmatrix} V_{r,1} \\ \vdots \\ V_{r,7} \end{pmatrix} = \begin{pmatrix} \cos\theta_1 \sin\phi_1 & \cos\theta_1 \cos\phi_1 & \sin\theta_1 \\ \vdots & \vdots & \vdots \\ \cos\theta_7 \sin\phi_7 & \cos\theta_7 \cos\phi_7 & \sin\theta_7 \end{pmatrix} \begin{pmatrix} V_x \\ V_y \\ V_z \end{pmatrix} \quad (1)$$

$$\mathbf{V}_r = \mathbf{D}\mathbf{U}. \quad (2)$$

Here, $V_{r,i}$ is the radial velocity measured by the ith beam and θ_i and ϕ_i are the elevation and azimuth (angle east of north, and noted in Figure 4) of the ith beam. The components V_x, V_y, and V_z of the vector velocity are the eastward (zonal), northward (meridional), and upward components (see Table 1). This overdetermined set of equations can be solved for the vector velocities using a pseudoinverse, i.e.,

$$\mathbf{U} = \left(\mathbf{D}^{\mathrm{T}}\mathbf{C}^{-1}\mathbf{D}\right)^{-1}\mathbf{D}^{\mathrm{T}}\mathbf{C}^{-1}\mathbf{V}_r \quad (3)$$

where $\mathbf{C}^{-1}$ is the covariance matrix of the measurements. This procedure was used in 1.5 km altitude bins to produce vector velocities. These winds are shown in Figure 5, interpolated to a much finer altitude grid. The winds show the clear wave

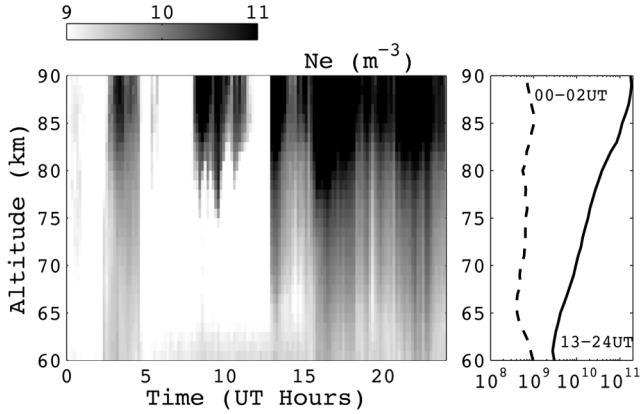

Figure 3. (left) Median electron density (N_e) from all beams in 5-km altitude bins from 0000 to 2400 UT on 23 April 2008. (right) Median over the 1300–2400 UT period (solid) and 0000–0200 UT period (dashed).

motion evident in the radial velocity measurements with the zonal and meridional wind patterns out of phase by ~90°. This motion will be investigated in section 4 when we analyze the wave properties.

3.4. Spectral Widths

[16] The fits to the spectra provide spectral widths in addition to radial velocities. Two spectral widths are derived, one associated with incoherent scatter and another associated with broadening processes like turbulence (see Appendix B for details). While incoherent scatter spectral broadening in the mesospheric region has in the past been associated with turbulence [e.g., *Chau and Kudeki*, 2006], to our knowledge this is the first time that a procedure like that described in Appendix B has been applied to incoherent scatter measurements of the *D* region. The half-power half-width (HPHW) for the Lorentzian *D* region incoherent scatter spectra neglecting the presence of negative ions, dust, and other charged particles, and assuming thermal equilibrium between ions, electrons, and neutrals, is given by equation (C13). Interpreting incoherent scatter spectral widths in the mesospheric region quantitatively is difficult because of the ambiguities associated with temperatures, collision frequencies, and the

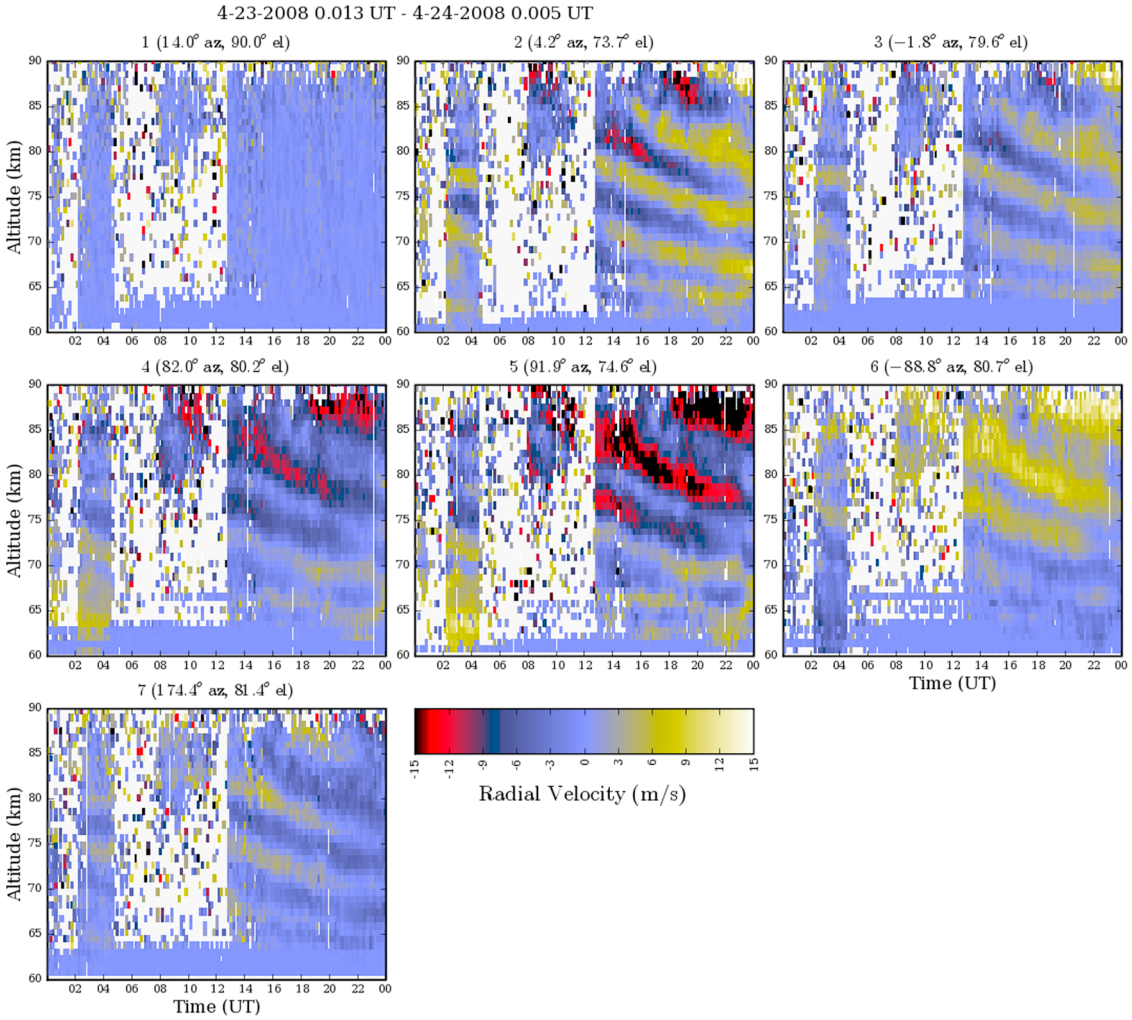

Figure 4. Radial velocity measurements for all seven beams for the full 24 h period on 23 April 2008. "White" areas are regions where ionization was not sufficient to measure Doppler velocities.

Table 1. Gravity Wave and Background Parameters Commonly Referred to in This Paper

Symbol	Definition
$\mathbf{U} = (U, V, W)$	background neutral wind vector (zonal, meridional, vertical)
(u', v', w')	wind perturbation (zonal, meridional, vertical)
$\mathbf{V} = (V_x, V_y, V_z)$	Total wind vector, i.e., $(V_x, V_y, V_z) = (U, V, W) + (u', v', w')$
$(\tilde{u}, \tilde{v}, \tilde{w})$	scaled wind perturbation, i.e., $(\tilde{u}, \tilde{v}, \tilde{w}) = (u', v', w') \exp(-z/2H)$
U_H	horizontal background wind in the direction of wave propagation
H	atmospheric scale height
$f = 2\Omega \sin\theta$	inertial (Coriolis) frequency, where Ω is the Earth's rotation rate and θ is latitude
N	Brunt-Väisälä frequency
$\lambda_x, \lambda_y, \lambda_z$	wavelengths (zonal, meridional, vertical)
$\mathbf{k} = (k, \ell, m)$	wave number vector (zonal, meridional, vertical), equal to $(\frac{2\pi}{\lambda_x}, \frac{2\pi}{\lambda_y}, \frac{2\pi}{\lambda_z})$
$k_H = \sqrt{k^2 + \ell^2}$	horizontal wave number
$\lambda_H = 2\pi/k_H$	horizontal wavelength
$\omega_r = 2\pi/\tau$	ground-based (observed) frequency and period
$\omega_{Ir} = 2\pi/\tau_I$	intrinsic frequency and period, i.e., $\omega_{Ir} = \omega_r - \mathbf{k} \cdot \mathbf{U}$

presence of negative ions and smoke particles, but has been the subject of several studies [e.g., *Tepley and Mathews*, 1978; *Tepley et al.*, 1981; *Rietveld and Collis*, 1993; *Chau and Kudeki*, 2006; *Strelnikova et al.*, 2007; *Raizada et al.*, 2008].

[17] The spectral HPHWs are shown for the vertical-looking beam in the top panel of Figure 6, averaged over 30 min and 3 km in altitude. The widths increase exponentially with altitude from a few Hertz at low altitudes to over

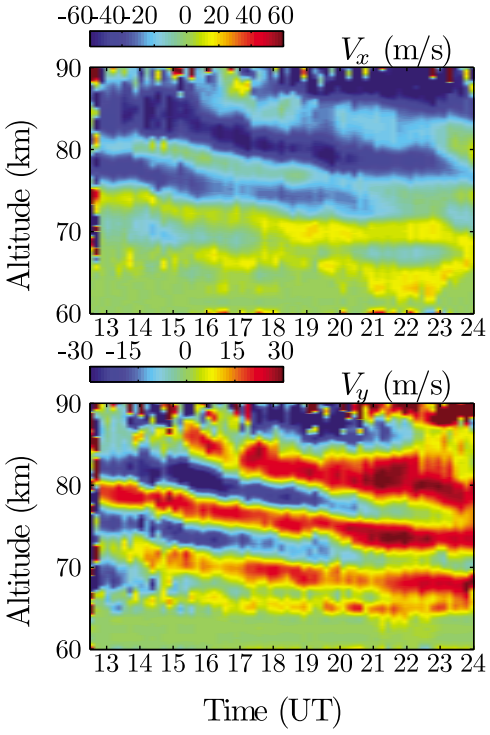

Figure 5. (top) Eastward (V_x) and (bottom) northward (V_y) total winds from 60 to 90 km for the period 1200–2400 UT on 23 April 2008. Note the different scales for the two plots.

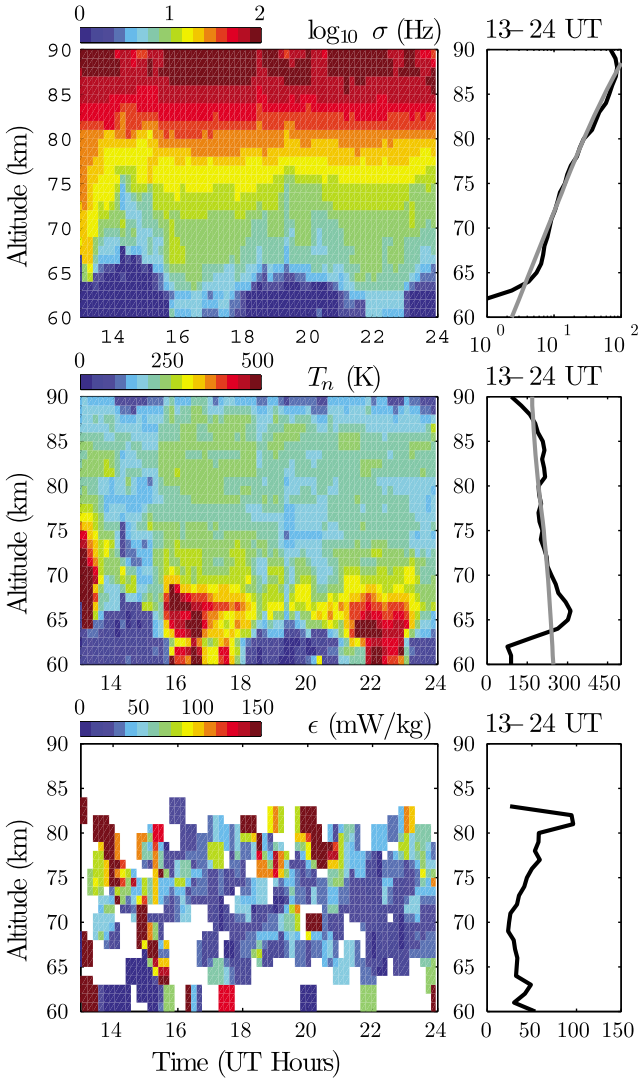

Figure 6. (top) Median Lorentzian half-power half-width in Hertz from the vertical-looking beam from 1300 to 2400 UT. The line plot shows the median over the period (black) along with the MSIS-predicted result (gray). (middle) Derived temperature using MSIS collision frequencies. The line plot shows the median T_n (black) and the MSIS T_n (gray). (bottom) Turbulence energy dissipation rate ϵ derived from the Gaussian component of the fit. The line plot shows the median from 1300 to 2400 UT.

100 Hz at 85–90 km. The widths are fairly uniform in time, although there is some apparent periodic modulation most evident at the lower altitudes. Because of the dual-dependence of the spectral width on the collision frequency and temperature, we have run the NRLMSISE-00 [*Picone et al.*, 2002] empirical model for these conditions. The MSIS-predicted spectral width is shown as the gray line in Figure 6 (top). In these calculations, we assume an ion mass of 30 amu (NO^+) and calculated collision frequencies using the expression given by *Hill and Bowhill* [1977]. The MSIS-predicted spectral widths increase with altitude exponentially with a fairly constant scale, which agrees with the scale of the measurements above about 73 km. Below that altitude, the

measured spectral widths show a "hump" before decreasing again below 62 km. This hump is most likely a spectral broadening due to the presence of negative ions [e.g., *Mathews*, 1978; *Tepley et al.*, 1981; *Raizada et al.*, 2008]. Note that a spectral broadening of a factor of 2 implies a negative ion to electron ratio of $\lambda \approx 1$, as theory predicts a spectral broadening of $\sim 1 + \lambda$ [e.g., *Mathews*, 1978].

[18] The spectral widths measured via *D* region incoherent scatter are sensitive to gravity wave effects through both collisional (neutral density) and temperature fluctuations. These fluctuations are readily observed in individual-beam measurements of spectral widths. However, as will be discussed later, these fluctuations are difficult to interpret both because of the variety of processes that can cause spectral width perturbations as a gravity wave propagates (including, for example, negative-ion concentration fluctuations due to modulations in O_2 attachment reactions driven by gravity wave temperature fluctuations [e.g., *Turunen*, 1996]) as well as effects like wind-shear, turbulence, and beam-broadening [e.g., *Hocking*, 1985].

[19] Apparent temperatures have been extracted from the spectral widths using the collision frequencies predicted by MSIS. These are shown in Figure 6 (middle) as a color plot and a median over the entire window. The temperatures above 73 km are close to the MSIS values, with MSIS T_n being only slightly colder. Below that altitude, the apparent temperatures increase because of the negative ion effects as already discussed. These temperatures should not be considered accurate in this region. One interesting aspect of these derived temperatures is the higher temperatures observed between 75 and 85 km between 1600 and 1800 UT as compared to the temperatures before and after this point. This temperature anomaly is likely real and represents a ~50 K variation in T_n in time. The Brunt-Väisälä frequencies can also be derived from the temperatures. From ~75 to 80 km, the Brunt-Väisälä period is very close to the value given by MSIS, with a period near 5 min. In the remainder of this paper, we assume that the Brunt-Väisälä period is constant at this value, which is not expected to be strictly true but a reasonable assumption given the expected variation in the range ~4–6 min [e.g., *Collins et al.*, 1996].

[20] Figure 6 (bottom) shows the turbulence energy dissipation rate (ϵ) determined from the Gaussian component of the spectral fit (see equation (B7) in Appendix B for details), along with the 12-h median profile. White areas indicate either regions of very low ϵ or regions where errorbars on the Gaussian component were large. ϵ increases with altitude from about 30 mW/kg at 65–70 km to ~70 mW/kg at ~80 km. There is some temporal variation in the derived ϵ, such as an enhancement at ~2000 UT at the higher altitudes.

[21] Note that we have neglected broadening processes due to beam and shear-broadening by the winds [e.g., *Nastrom*, 1997]. This is justified for the vertically directed beam, where the maximum beam-broadening effect for PFISR is ~0.75 m/s (~2.5 Hz HPHW), or a corresponding apparent energy dissipation rate of ~6 mW/kg.

4. Analysis

4.1. Polarization Analysis

[22] The polarization relationship relating the scaled zonal and meridional wind perturbations for an atmospheric gravity wave can be written as [e.g., *Fritts and Alexander*, 2003]

$$\tilde{u} = \left(\frac{i\omega_{Ir}k - f\ell}{i\omega_{Ir}\ell + fk}\right)\tilde{v} \tag{4}$$

where the relevant parameters are defined in Table 1. Here, the zonal and meridional wave velocities have been scaled to account for their exponential growth with altitude due to the decrease in the background density. This analysis assumes perturbations varying in space and time as described in Appendix C1. It also assumes that the observations represent a single wave propagating vertically through the field-of-view. But given $\lambda_z < 15$ km and $\tau > 10$ hr (see Figure 5), this implies that $\lambda_H > 500$ km, which describes a nearly horizontally propagating wave, as we discuss later in this paper. Therefore, the coherence of the wave in Figure 5 is more indicative of a coherent source than of a single wave.

[23] Equation (4) describes an elliptically polarized wave rotating in the anticyclonic direction ($\tilde{v}$ leading $\tilde{u}$ in altitude and time). For the case where the intrinsic frequency approaches the local inertial frequency, the wave becomes circularly polarized. Otherwise, the $\tilde{u}$-$\tilde{v}$ hodograph provides information both on the propagation direction (orientation of the hodograph, with a π ambiguity) and on the ratio of the intrinsic (ω_{Ir}) to inertial (f) frequency (ratio of major to minor axes of the ellipse), and has become a frequently used analysis tool for the characterization of IGWs [e.g., *Cho*, 1995; *Gavrilov et al.*, 1996; *Hu et al.*, 2002], although it can be affected by wind shear perpendicular to a wave's propagation direction [*Hines*, 1989]. Measurements of temperature perturbations and/or vertical wind variations can also be used as supplemental information for determining a wave's propagation characteristics, as discussed in Appendices C2 and C3. Note that although this PFISR experiment has significant horizontal coverage, it cannot resolve λ_H directly as has been previously done [*Nicolls and Heinselman*, 2007], because λ_H is much larger than the horizontal extent of the measurements in this case (see Figure 1).

[24] The background winds were determined by low-pass filtering the winds in Figure 5 to remove wave perturbations with vertical wavelengths less than 15 km. These background winds are then subtracted from the data to obtain the wave perturbations. They are also used to determine the intrinsic frequency and nondimensional wave amplitudes later in this paper. The wave horizontal velocities are shown in Figure 7 (top) in 2-h intervals (note that the fundamental range resolution of this data set is 1.5 km and the data has been interpolated before filtering as described previously). Above 85 km, the broadened spectra make it difficult to determine the winds. Wave amplitudes increase rapidly with altitude, especially during the earlier times. This is the expected result from the conservation of energy for a single wave. In particular, wave horizontal velocities grow from less than 10 m/s at 65 km to nearly 30 m/s at ~80 km for the 1400–1600 UT case. However, the wave amplitudes are approximately constant with altitude for $z > 75$ km at 1600–1800 UT, for $z > 70$ km at 1800–2200 UT, and for $z > 65$ km at 2200–2400 UT. A constant wave amplitude with altitude implies wave saturation for a single wave [e.g., *Fritts and Alexander*, 2003]. This occurs when a wave's nondimensional amplitude becomes large enough that it undergoes convective or

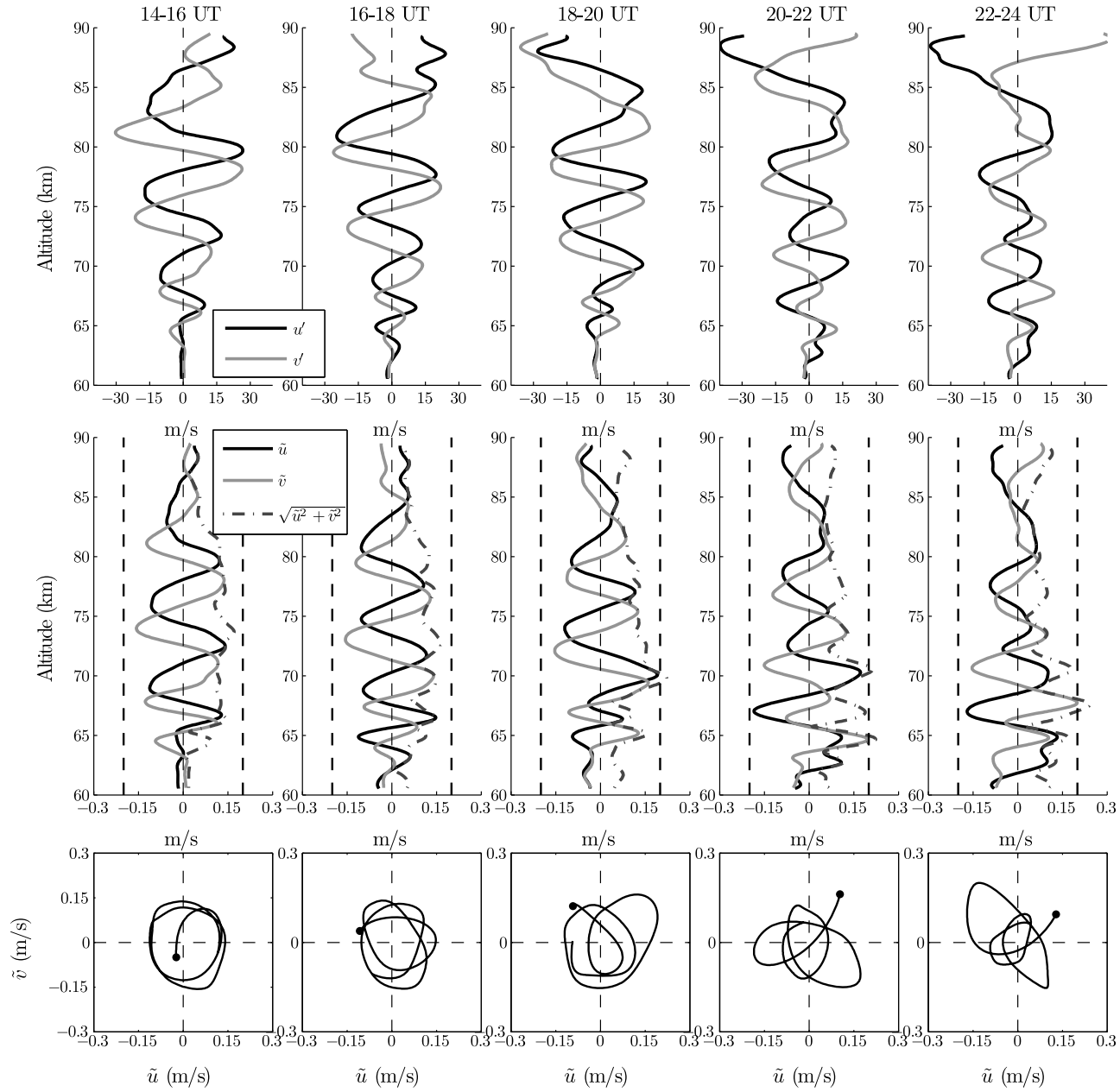

Figure 7. (top) Wave horizontal velocities in the zonal (u', black) and meridional (v', gray) directions for each 2-h interval. (middle) Wave horizontal velocities scaled by $\exp[-(z - z_0)/2H]$ where $z_0 \approx 15$ km and $H \approx 6$ km. The blue dashed-dotted line is the scaled magnitude, $\tilde{u}_H$. Dashed lines show exponential amplitude growth with altitude. (bottom) Hodographs of $\tilde{u}$ and $\tilde{v}$ from 65 to 80 km. The dots denote $\tilde{u}$ and $\tilde{v}$ at $z = 65$ km.

dynamical instabilities. Note that at early times the perturbations vary sinusoidally with altitude, indicative of a coherent wave packet. At later times (especially 2200–2400 UT); however, the perturbations do not vary as a single sinusoid in altitude. This indicates the presence of other waves, smaller-scale waves, and/or other secondary effects created by wave instabilities [e.g., *Fritts et al.*, 2006].

[25] To investigate whether or not wave saturation might have occurred, we plot the wave horizontal velocities scaled by $\exp[-(z - z_0)/2H]$ in Figure 7 (middle), assuming a scale height $H = 6$ km and $z_0 = 15$ km (nominal wave source altitude). If no wave dissipation occurs, then a wave's amplitude will not vary with altitude in these plots. The scaled wind perturbation amplitudes (i.e., $\tilde{u}_H = \sqrt{\tilde{u}^2 + \tilde{v}^2}$) are shown by the dashed-dotted curves in Figure 7. They are seen to decrease at some altitude for all times of interest, implying that the wave might be saturated above that altitude. This occurs beginning at about 72 km in the first time period (1400–1600 UT) and moves progressively lower in altitude as time goes on, reaching ~67 km at 2200–2400 UT. The implications of this effect will be investigated later. We note that u' and v' being constant with altitude does not necessarily indicate wave saturation for nearly horizontally propagating waves (see section 5.3). However, we

will show later (via calculation of the nondimensional wave amplitudes) that the waves are saturated in this case.

[26] Figure 7 (bottom) show hodographs of the scaled horizontal wind perturbations for each 2-h interval from 65 to 80 km. The $\tilde{u}$-$\tilde{v}$ hodographs show a clockwise rotation with altitude, indicating that the meridional wind perturbations are leading the zonal wind perturbations in altitude/time. This phase relationship is consistent with an upward propagating inertia-gravity wave in the Northern Hemisphere (anticyclonic rotation).

[27] As mentioned earlier, the orientation of the hodograph ellipses can be used to determine the direction of wave propagation to within a 180° ambiguity in direction. The hodographs in Figure 7, especially at the early times when they are well-behaved, are nearly circular, with perhaps a slight extension in the meridional direction. However, in general, the hodographs are not at all uniform in time; one would obtain very different angles of propagation from analysis of the five different hodographs. For example, compare to the IGW reported by *Li et al.* [2007], where the elliptical orientation is very clear and consistent at different times, and where the vertical wavelength is much larger, making the analysis less error-prone. This difficulty may be due in part to measurement errors in the wave amplitudes and in removing background winds. However, it may represent real variability in wave behavior with altitude and time, due to either varying wave properties with altitude or the presence of secondary/smaller-scale waves. This is likely why the hodographs at 2000–2400 UT are so nonuniform with altitude. Note also that the hodographs from 1400 to 2000 UT below the wave saturation altitudes look reasonably uniform and circular. For these reasons, a different approach will be used to infer the direction of propagation.

[28] Wave amplitudes were fit in time for the period beginning at 1200 UT at each altitude with the equations for an ellipse,

$$\begin{aligned}\tilde{u} &= A\cos\left[-\frac{2\pi(t+t_0)}{\tau}\right]\cos\phi - B\sin\left[-\frac{2\pi(t+t_0)}{\tau}\right]\sin\phi \\ \tilde{v} &= A\cos\left[-\frac{2\pi(t+t_0)}{\tau}\right]\sin\phi + B\sin\left[-\frac{2\pi(t+t_0)}{\tau}\right]\cos\phi\end{aligned} \tag{5}$$

where A and B are the major and minor axes of the ellipse, respectively, t is time, t_0 is a starting time offset, τ is the period, and ϕ is a phase angle denoting propagation direction north of east.

[29] An estimate of the average period, τ, was determined via a median of the results from 70 to 80 km altitude (where the quality of the data was the highest):

$$\tau = 10.5 \pm 0.5 \text{ hrs} \tag{6}$$

where the error bar corresponds to the standard deviation of the samples. This large error occurs because (1) the wave period is long compared to the observation window, and thus it is difficult to determine an accurate period, and (2) the ground-relative period actually changes with altitude. In particular, the wave period was seen to change from ~13 h at 60 km to ~10 h at 85 km. For future calculations in this study, we will assume that the period decreases linearly between those two altitudes. Note that the local inertial period is $2\pi/f \sim 13.2$ h.

[30] These results also lead to an estimate of the phase angle as

$$\phi = \pm 100^\circ \pm 30^\circ. \tag{7}$$

The large error on the phase angle is a result of the fact that the wave is propagating very close to the inertial frequency and is thus nearly circularly polarized (because the background winds are small; see the next section). The ratio of the major to minor axes of the elliptical fits give an estimate of the ratio of the intrinsic to the inertial frequency. We find this value to be $\omega_{Ir}/f \simeq 1.1$–1.3 for all altitudes of interest.

4.2. Mean (Background) Winds

[31] Estimates of the background or mean zonal and meridional winds, U and V, respectively, are shown in Figure 8 for the same time intervals as in Figure 7. While the mean winds were also determined using the method described in section 4.1 (interpolating and filtering the measured vector velocities), a slightly different approach was used for the winds presented here, which gives three independent estimates of the winds. For each look direction, with the exception of the vertical, radial velocities were low-pass filtered to remove the fluctuations in the measured winds due to the presence of the gravity wave. Three estimates of both U and V were constructed using the three different look directions in both the meridional and zonal directions.

[32] These three wind estimates are represented by the black lines in Figure 8. The gray lines are the average of those curves, which in general agree extremely well, especially at lower altitudes. The variation between the curves can be considered the error estimate on the derived winds. Note that this method ignores vertical winds, which is justified because the observed vertical velocities are very small (~<1 m/s).

[33] The background winds show some interesting and important trends. Both the zonal and meridional winds are small below 70 km. Above that altitude, the zonal wind increases strongly in the westward direction, to a value of ~40 m/s. The winds at the lower altitudes accelerate slightly eastward as a function of time, to a peak of about 10 m/s for the last time bin. The meridional wind remains small until ~1800–2000 UT, at which point it accelerates in the northward direction above 65 km to a value of 10–20 m/s. Also plotted in Figure 8 are the winds predicted by the 2007 Horizontal Wind Model (HWM) [*Drob et al.*, 2008] for each 2-h interval as dashed black lines. This empirical model includes tidal motions, planetary waves, and other effects. In the zonal direction, the HWM winds show similar trends: small, eastward winds below 70 km and westward winds above that level, although the observed westward winds above 70 km are 20–40 m/s larger than the HWM winds. In the meridional direction, the winds agree extremely well at all altitudes after 2000 UT when the observations show a brief but clear northward acceleration. Prior to that time, the model winds predict values close to 10–15 m/s below 70 km, whereas the observations show winds very close to zero. There is also disagreement at the higher altitudes at the earlier times, when the measured meridional winds show a southward excursion. We will show later that the dynamics of the dissipating IGW and its relationship to changes in the

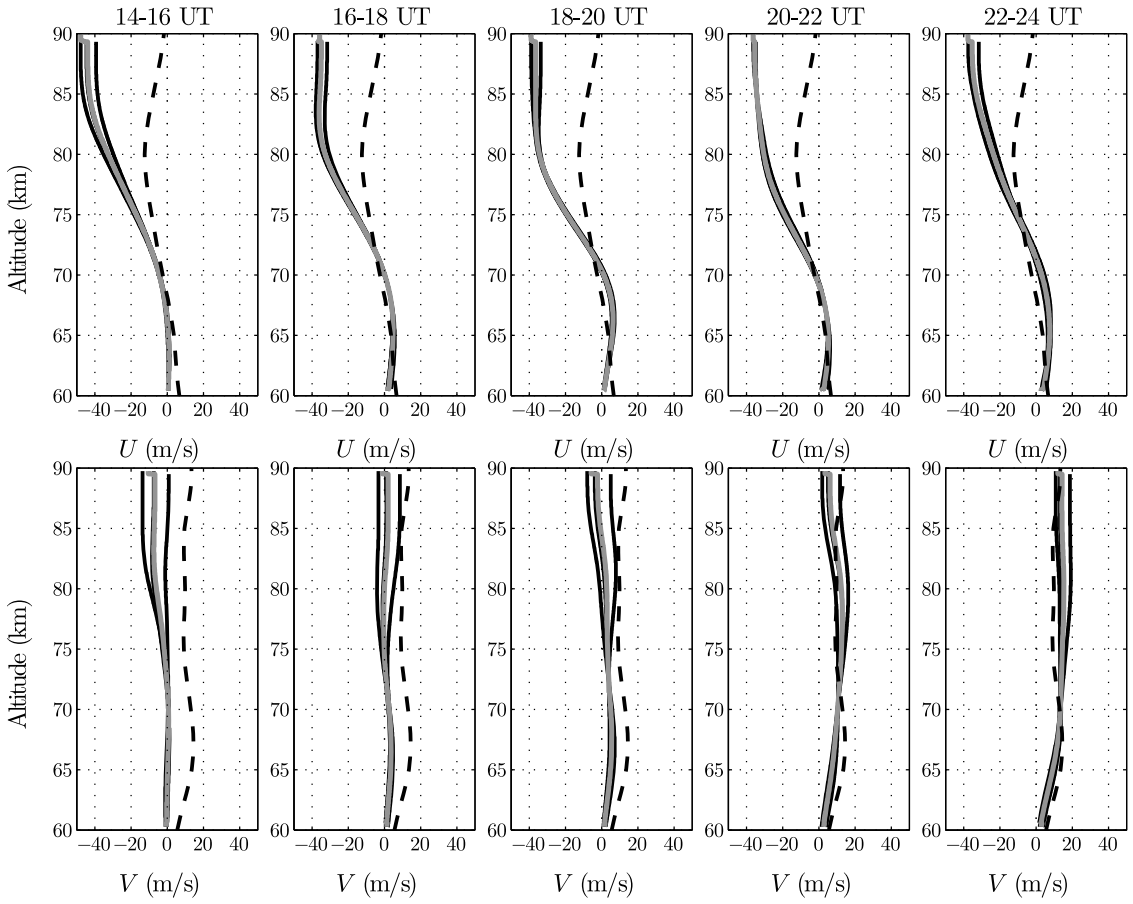

Figure 8. (top) Mean zonal and (bottom) meridional winds from 1400 to 2400 UT in 2-h intervals. Solid black lines are the three independent estimates (different look directions) and gray lines are the means of the three estimates. The dashed line is the HWM quiet time wind prediction.

background winds as a function of altitude and time are reasonable.

4.3. Vertical Wavelength

[34] By definition, the variation of a freely propagating wave's amplitude with altitude is proportional to exp(*imz*). Therefore we determine the vertical wavelength $\lambda_z = 2\pi/m$ here by locating the maxima and minima in the wave perturbations from each beam (not including the vertical beam) independently. The altitudes of the minima and maxima were differenced and doubled to determine the vertical wavelength, and an average altitude was assigned. The results are shown in Figure 9 (top) for the 2-h intervals previously discussed. The black points show all measurements from all beams, and the blue lines represent medians in 5 km running bins, separated by 2.5 km. Errorbars correspond to standard deviations. The red lines and the lower panels will be discussed later. We see that the vertical wavelengths increase with altitude, from less than 5 km below 65 km altitude to over 10 km at 80–85 km. There are some "kinks" in the average curves, where the vertical wavelength appears to change quite rapidly. We note that variations in vertical wavelength are indicative of variations in the background winds [e.g., *Vadas and Nicolls*, 2008, 2009] because λ_z is directly related to ω_{Ir} (not ω_r) through the dispersion relation. We will relate these measurements to wind variations later.

4.4. Direction of Propagation

[35] As discussed earlier, a typical approach used to derive the propagation direction for IGWs within a factor of π is to use the polarization relationship between $\tilde{u}$ and $\tilde{v}$ (i.e., the orientation of the $\tilde{u}$-$\tilde{v}$ ellipse). To resolve the 180° ambiguity, additional information must be incorporated. For lidar measurements [e.g., *Hu et al.*, 2002; *Li et al.*, 2007], this has typically involved the incorporation of temperature perturbation information, which has a prescribed phase relationship with u' and v' given by the gravity wave polarization relationships [e.g., *Fritts and Alexander*, 2003].

[36] In the case of incoherent scatter, we do not directly measure the temperature. We do, however, measure spectral widths, which are proportional to temperature and inversely proportional to collision frequency. As noted earlier, perturbations in the spectral widths were readily observed, implying that gravity wave phase information can be extracted from those measurements. In Appendix C3, we derive the expected phase relationships between the measured IS spectral widths and the horizontal wind perturbations. This phase relationship allows one to extract the direction of propagation of the IGW with no ambiguities; however, the amplitude of the perturbations is very small, on the order of a few percent (and only when the intrinsic frequency is sufficiently larger than the inertial frequency). Radar measurements of spectral widths

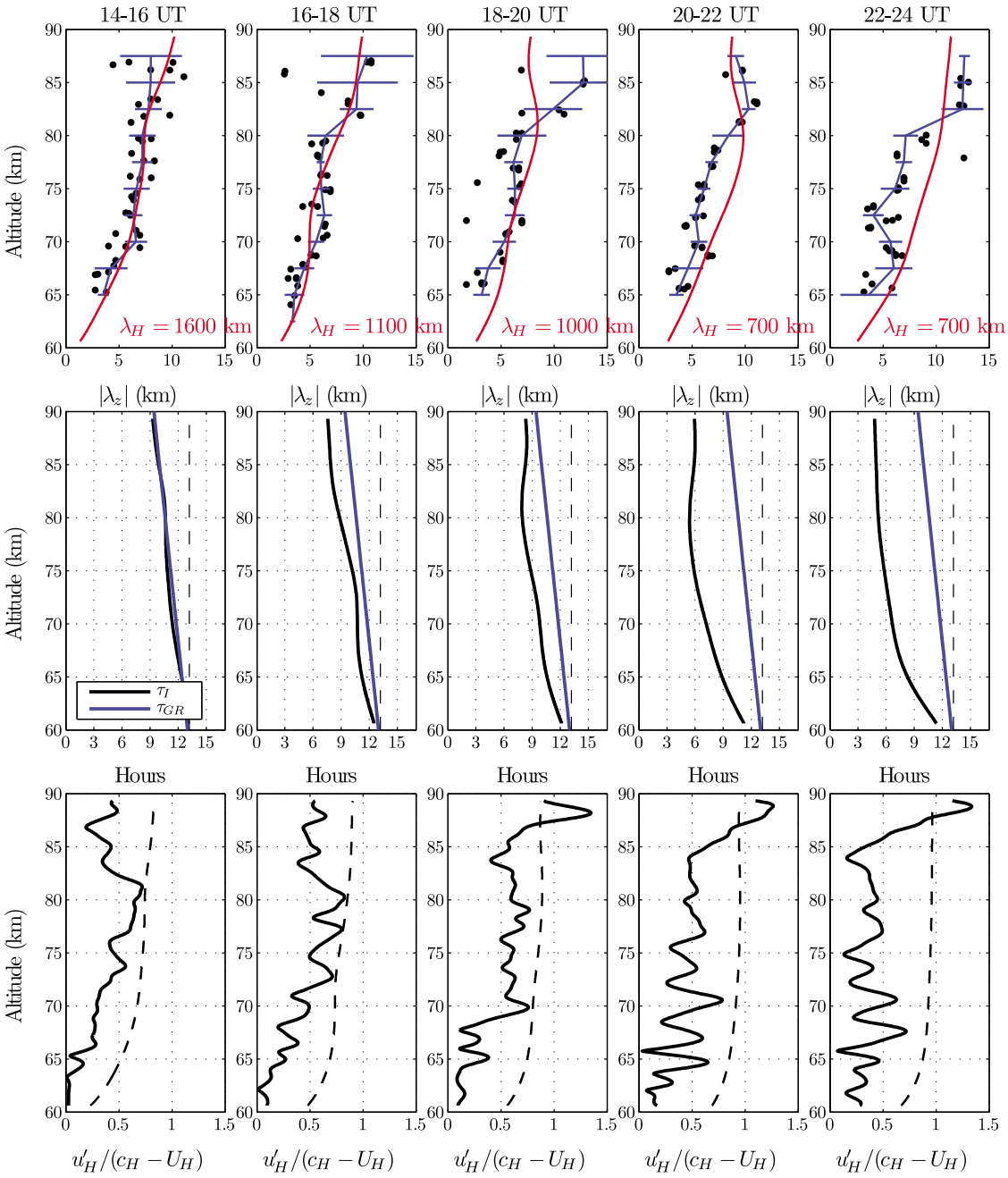

Figure 9. (top) Measured vertical wavelengths from all beams (black points), median and standard deviation in 5-km altitude bins (blue), and dispersion relation prediction (red, see text for details). (middle) Ground-relative period (blue) and intrinsic period (black) in hours. The dashed line corresponds to the inertial period for the Poker Flat location. (bottom) Nondimensional wave amplitude (solid) and condition for dynamical stability (equation (12), dashed).

are sensitive to effects such as beam and shear broadening [e.g., *Sloss and Atlas*, 1968; *Hocking*, 1985; *Nastrom*, 1997; *Nastrom and Eaton*, 2006], which depend both on the size of the scattering volume and the magnitude of the winds and wind shears. An analysis of the spectral width perturbations shows that they are correlated with wind shear, an effect observed before with the EISCAT VHF and UHF ISRs, which are systems with comparable beam size as PFISR [*Collis and Rietveld*, 1998]. These effects are particularly strong in off-vertical looking beams. As such, we have attempted to remove the main source of beam broadening by background, uniform, horizontal winds by utilizing only the vertical beam. This effect has a magnitude of approximately $\zeta|u_0|/\sqrt{3}$ for a vertically directed beam [*Nastrom*, 1997], where $|u_0|$ is the background wind magnitude and ζ is the beam half-width. Shears in the horizontal wind will also induce broadening; however, these terms are in general smaller, and they can be compensated for using PFISR's capability to determine the shears.

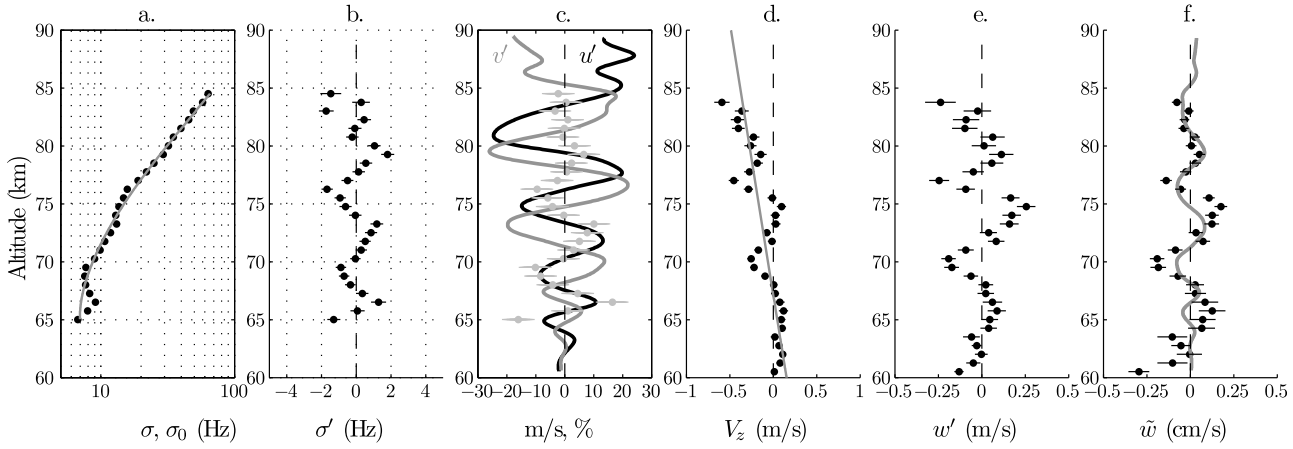

Figure 10. For the period from 1600 to 1800 UT: (a) Average spectral width measurements (black points) and polynomial fit (gray line); (b) spectral width perturbations, in Hertz; (c) zonal (black) and meridional (gray) wind perturbations, along with percentage spectral width perturbations (light gray points with error bars); (d) vertical velocity measurements (black points with error bars), V_z, along with a linear fit to the background mean vertical W (gray line); (e) vertical velocity perturbation $w' = V_z - W$; (f) $\tilde{w} = w' \exp[-(z - z_0)/2H]$, along with the theoretical curve using equation (C12) (solid).

[37] In Figure 10a, we show the measured spectral widths for a 2-h period (1600–1800 UT) along with a polynomial fit, which is taken to be the background spectral width. These are used to produce estimates of the spectral width perturbations, which are shown in Figure 10b. Clear wave motion is seen with 1–2 Hz amplitude. These perturbations do not grow exponentially in altitude, as expected, since the spectral width grows exponentially with altitude if the temperature is constant (see equation (C1)). In Figure 10c, we show the percentage spectral width perturbations (light gray points with error bars) on the same axes as the wind perturbations, $\tilde{u}$ and $\tilde{v}$. Above about 75 km, the perturbations are essentially zero. Below 75 km, however, the perturbations have the same vertical wavelength and are very nearly in phase with the zonal wind perturbations. Referring to Appendix C3, these observations imply a predominantly southward propagating wave. While there is some ambiguity in this result, as the phase varies somewhat, this result is in rough agreement with the previous polarization analysis that indicated that the wave was propagating mainly meridionally (northward or southward).

[38] In addition to equation (4), gravity wave theory also predicts the polarization relations which relate the phase and amplitude of a wave's vertical wind perturbations to its horizontal wind perturbation components when f is important (see Appendix C2 for the small λ_z expressions, and (S. L. Vadas, Compressible f-plane solutions to local body forces and heatings: 1. Initial value and forced/heated solutions, submitted to *Journal of the Atmospheric Sciences*, 2010a) for the larger λ_z, compressible expressions). These relations can be used to determine the direction of wave propagation when the vertical velocities can be adequately measured. Measurements of vertical velocities to precisions necessary for these types of calculations are in general very difficult; however, the spectra in the 70–80 km altitude range are sufficiently narrow that for a 2-h average reliable results can be obtained in this experiment. An example is shown in Figure 10d where we plot the (total) measured vertical velocity (V_z). Here, the vertical velocity measurements have been averaged for 2 h using a weighted mean, and the error bars reflect the expected error on the mean. The magnitude of the average vertical velocity, W, increases approximately linearly in altitude from ~0 m/s to ~0.5 m/s from 60 to 80 km, possibly indicative of the vertical variation of a tide or planetary wave. On top of this linear trend are oscillations which grow nearly exponentially with altitude up to 70–75 km (third panel), as expected for a single, freely propagating GW [e.g., *Hines*, 1960].

[39] Figure 10f shows the scaled vertical velocities. The slower increase with altitude above ~75 km is consistent with Figure 7, and indicates that the IGW might be saturated. The theoretical curve given by equation (C12) is also shown in this panel (assuming southward propagation). This curve is quite sensitive to ω_{Ir} and N. For example, if N is increased by 1 min from 5 to 6 min, the predicted perturbation amplitudes increase by a factor of about 1.5. The comparison of the data with this curve shows that the oscillations of w' are well correlated with those of u' and v', implying that w' is primarily the vertical velocity component of the IGW. There are also additional smaller-scale fluctuations from $z \sim 70$ to 75 km which are not resolved sufficiently due to the limited range resolution. This is also the altitude where the horizontal velocity components became constant with altitude, implying wave saturation (see Figure 7). We will show later that this IGW does indeed saturate at this altitude and time. Therefore it is quite likely that these smaller-scale fluctuations in w' are related to the smaller-scale waves which arise from this dissipative process. In addition to the vertical velocities being small at lower altitudes because of their exponential increase with altitude, the vertical velocities are also small there because the intrinsic wave period is closer to the inertial period, since $\omega_{Ir} \rightarrow f$ implies $w' \rightarrow 0$, regardless of the values of u' and v' (see equation (C12)).

[40] Using Figures 10c–10f and the phase relationship between the different components of the wind perturbations given in Appendix C2, we now determine the propagation

direction of the IGW. From Figure 10f, we note that w' is generally anticorrelated with v'. For example, the minima in w' at 70 km corresponds to a maxima in v'. This subsequently corresponds to a lagging of u' by ~90°, corresponding again to approximately southward wave propagation (see Appendix C2). While there is again some uncertainty in this approach, this is yet another piece of evidence that suggests southward propagation. Thus in the absence of additional information, we conclude that this IGW is propagating approximately southward.

4.5. Horizontal Wavelength and Intrinsic Parameters

[41] The horizontal wavelength was estimated using the dispersion relation for IGWs by solving for $k_H = \sqrt{k^2 + l^2}$. This has been done by *Liu and Meriwether* [2004] and is also the approach taken by *Li et al.* [2007]. The relation is given by

$$k_H = \frac{\omega_r U_H}{U_H^2 - N^2/m^2} \pm \sqrt{\left(\frac{\omega_r U_H}{U_H^2 - N^2/m^2}\right)^2 - \frac{\omega_r^2 - f^2}{U_H^2 - N^2/m^2}}, \quad (8)$$

where the symbols are again defined in Table 1. Using this equation and assuming a single IGW from 60 to 85 km (i.e., assuming no contamination from secondary waves and other motions created during wave saturation), we compute the horizontal wavelength $\lambda_H = 2\pi/k_H$ as a function of altitude using the measured vertical wavelengths and assuming roughly southward propagation to determine the background wind in the direction of wave propagation. We do this for each 2-h time period from 1400 to 2000 UT and find that the calculated horizontal wavelength decreases steadily as a function of time, from about 1600 km at 1400–1600 UT to ~700 km at 2000–2200 UT. We do not evaluate the average λ_H for 2200–2400 UT because there are clearly multiple waves present at that time, thereby yielding an inaccurate value of λ_z for the IGW, since we are unable to separate the different wave components.

[42] While other parameters (e.g., N or ω_r) that have been assumed to be fixed in time could certainly be changing, it is more likely that this dramatic decrease in λ_H is a result of dynamical processes. First, smaller λ_H waves with similar frequencies (excited by the same geostrophic adjustment process) will arrive later because they have smaller vertical group velocities. This effect has been confirmed by a recent modeling study of IGWs excited by a geostrophic adjustment (S. L. Vadas, Compressible f-plane solutions to local body forces and heatings: 2. Gravity wave, acoustic wave, and mean responses, submitted to *Journal of the Atmospheric Sciences*, 2010b); in that case, λ_y decreased from ~1300 to 850 km (a 45% decrease) in 12 h. In the results shown in this case study, λ_y decreases by 45% in 4–6 h Therefore although some portion of the decrease may be due to this effect, it cannot account for all of it. Second, for a southward propagating GW ($\ell < 0$) with a small horizontal phase speed, λ_H can change significantly along its propagation path if the meridional wind varies in the meridional direction. The ray trace equation that governs this change is $d\ell/dt = -\ell \partial V/\partial y$ (see Appendix D). In fact, we know that V increases at PFISR (see Figure 8), and this is likely a "local" effect, mainly caused by IGW saturation from 1400 to 2000 UT (as we discuss later, in section 5.1). This southward forcing decreases the northward wind to zero during these times. If we assume that this zero wind is centered in the region above PFISR with a value of ~10 m/s and a meridional extent of $\sim 2\lambda_y$ (covering a typical wave packet), then we can estimate the change in λ_y resulting from the gradient in the neutral wind. Since the wind is directed northward north of this region, then $\partial V/\partial y > 0$, and $|\ell|$ will decrease ($|\lambda_y|$ will increase) along its raypath as it nears the region above PFISR. We estimate $\Delta V \sim 10$ m/s over the meridional distance $\Delta y \sim \lambda_y$ and during the time $\Delta t \sim \lambda_y/c_y$, where $c_y \sim 10$ m/s. Then, the fractional change of the meridional wavelength is $\Delta|\lambda_y|/|\lambda_y| \sim 1$. This says that the IGW's wavelength was $\lambda_y \sim$ 700 km prior to reaching the zero wind region centered over PFISR; once it reached PFISR, λ_y increased to the observed values of 1600–1000 km. This makes sense, because the IGW's intrinsic frequency above PFISR is smaller at earlier times than at later times (see Figure 9). Since $\omega_{Ir} \sim \sqrt{k_H^2 N^2 + m^2 f^2}/m$, a smaller ω_{Ir} implies either a larger m (i.e., a smaller vertical wavelength) or a smaller k_H (i.e., a larger horizontal wavelength). Because m is not expected to change from this meridional wind gradient, ω_{Ir} can only decrease if λ_H increases. This result can be thought of in terms of the angle of propagation. In order to make ω_{Ir} smaller, the wave must propagate closer to the horizontal. But if λ_z remains constant, the only way this can occur is if the horizontal wavelength increases. Therefore we conclude that most of the decrease in time of λ_H can be explained by a meridional wind gradient. Some of the decrease may also be caused by the later arrival of the smaller λ_H IGWs from the same source.

[43] For that portion of λ_H that decreases because of the arrival of smaller λ_H waves from the same source later in time, we expect that λ_z would correspondingly decrease from ~6 km to ~4–5 km for zero winds. This decrease is not observed, which is due to the background winds increasing in the northward direction during this time interval (see Figure 8). This northward increase causes λ_z for these southward propagating smaller IGWs to increase because the waves are increasingly propagating against the background wind. Thus the trend that λ_H decreases but λ_z does not is qualitatively consistent with gravity wave theory.

[44] Given the horizontal wavelength, propagation direction, and background mean winds, we are now in a position to calculate a theoretical value of λ_z from the dispersion relation for inertia-gravity waves, and compare with the measured results. The vertical wavelengths calculated from the IGW dispersion relation,

$$m^2 = \frac{k_H^2 N^2}{\omega_{Ir}^2 - f^2} - k_H^2, \quad (9)$$

are shown as red lines in the top panel of Figure 9, which assumes a propagation direction of ~−80° and a λ_H that varies in time as indicated. Here, λ_H is the altitude average of the deduced horizontal wavelength as discussed in the previous paragraphs. A constant Brunt-Väisälä period of 5 min was used. The red curves agree with the data quite well for the

first three 2-h periods. The curves agree less well for 2000–2400 UT where $\lambda_H = 700$ km has been assumed (which is the 2000–2200 UT result). In this case, the theoretically calculated values of λ_z are larger than the measured results. This period of poorer agreement likely occurs because (1) the assumed value of λ_H is not valid for the IGWs present during this period, or (2) the small-scale (but reasonably large-amplitude) secondary gravity waves created from IGW saturation decreases the measured λ_z.

[45] For a fixed 2-h time period, Figure 9 shows that the vertical wavelengths increase with altitude as a result of the decreasing ground-based period and the fact that the background mean winds are strongly westward above 70 km (see Figure 8). The middle row of Figure 9 shows the ground-based period (blue), which is assumed to decrease linearly with altitude as discussed already, along with the inertial period (dashed lined) and the intrinsic period, $\tau_I = 2\pi/(\omega_r - k_H U_H)$. At the early times, the intrinsic period is approximately equal to the ground-based period because the meridional winds are small. As time progresses, the meridional winds increase in the northward direction, which causes ω_{Ir} to increase, since these waves are southward propagating. Because the observed average λ_z is approximately constant in time, ω_{Ir} increasing implies that λ_H must be decreasing in time, as discussed above.

[46] The assumed constancy of the ground-based period in time is a good assumption if the source of the waves (i.e., geostrophic adjustment) is located at a single point and if the intervening winds are very small. Otherwise, the ground-based periods of the waves that reach $z \sim 60$ km directly above PFISR would change with time over this 10 h period, especially if the semidiurnal tidal horizontal wind amplitude is greater than a few m/s. This change, however, is extremely difficult to determine for a wave with a ~10 h period using this 10–12 h data set. Hence we must assume that the ground-based periods are constant here. If they are not constant, then λ_H will be somewhat different for each 2-h time bin than that determined here.

5. Discussion

5.1. Wave Saturation

[47] In Figure 7 (middle), we showed evidence that this wave is saturated for the entire duration of the observation window. In this figure, the scaled wind magnitude (blue dashed-dotted line) decreases above 72 km for the 1400–1600 UT case. The altitude where the amplitude begins to decrease is seen to move steadily downward as time progresses. While these effects could be due to source variability and the fact that the wave is propagating almost purely horizontally, we will show evidence that the wave is indeed saturated, causing most of its momentum to be deposited into the background flow. For a southward propagating wave, saturation leads to an acceleration of the southward mean background wind. Examination of the background winds in Figure 8 shows that the meridional winds before 2000 UT are more southward than that predicted by HWM. In addition, the winds show a southward divergence above 72–75 km, corresponding to the approximate altitude where we see clear wave saturation effects. These observations imply that this saturated wave is pushing the mean flow southward by ~10–20 m/s. This makes sense theoretically. The acceleration of the background flow is [*Andrews et al.*, 1987]

$$F_b = -\frac{1}{\overline{\rho}} \frac{\partial\left(\overline{\rho}\,\overline{u'_H w'^*}\right)}{\partial z}, \tag{10}$$

where $\overline{u'_H w'^*}$ is the momentum flux of the wave and "*" denotes the complex conjugate. Since $\overline{u'_H w'^*} \simeq$ constant when a wave is saturated, the acceleration of the background wind is

$$F_b \simeq \overline{u'_H w'^*}/H. \tag{11}$$

Using $u'_H \simeq 25$ m/s and $w' \simeq 0.25$ m/s from Figure 10d at $z \sim 75$ km, this implies an acceleration of $F_b \sim 4$ m/s/hr. Averaged over 2 h, the net meridional wind change from this acceleration is then $\Delta V \sim -8$ m/s. At this altitude and time, Figure 8 shows that the background winds are more southward than that predicted by HWM by about 10 m/s. Therefore our estimate of the meridional wind change because of the saturating IGW, ΔV, agrees well with the background wind difference between the measurements and the HWM model winds.

[48] Although this result is illuminating, the HWM is not expected to capture all of the day-to-day variability inherent in the Earth's atmosphere. Therefore in order for us to understand how the acceleration of this wave affects the background wind, we need to directly compare the IGW amplitude with the background winds. It turns out that we need only compare the background wind before and after 2000 UT because the IGW amplitude decreases significantly after 2000 UT, as we will show. This implies that the acceleration from the dissipating IGW should be much smaller after 2000 UT. We can then difference the background winds before and after 2000 UT, and compare this to ΔV.

[49] After 2000 UT, the background winds are observed to shift northward. This is evident in Figure 8 but is made more clear in Figure 11 (left), where we show the background winds as a function of time. The zonal winds are relatively uniform for the whole time period. The meridional winds, on the other hand, suddenly increase by ~10–15 m/s in the northward direction around 20 UT. Thereafter, the meridional wind is reasonably constant in time. At 75 km, this increase is ~10–15 m/s, nearly equal to $-\Delta V$. In the right column of Figure 11, we show the wave horizontal velocities (u', v', and $u'_H = \sqrt{u'^2 + v'^2}$). Figure 11 (bottom) indicates that the wave amplitude is significantly reduced at $z > 70$ km beginning at about 1900 UT. Altogether, the IGW amplitude decreases by ~20 m/s (or ~70%) from before to after 2000 UT. Although the reason for this decrease is not known, one possibility is that because the IGWs have smaller λ_H at that time, they also have smaller horizontal phase speeds, making them more susceptible to critical level filtering in the stratosphere. Therefore it is possible that a portion of the wave packet is suddenly removed in the stratosphere from critical level filtering. It is also possible that the wave source changes on times scales of ~1 h, but this is less likely.

[50] In conclusion, then, while the IGW had a large amplitude while saturating, it accelerated the background flow to the south, changing the background meridional wind by $\Delta V \sim 8$ m/s every 2 h. Once the IGW was significantly

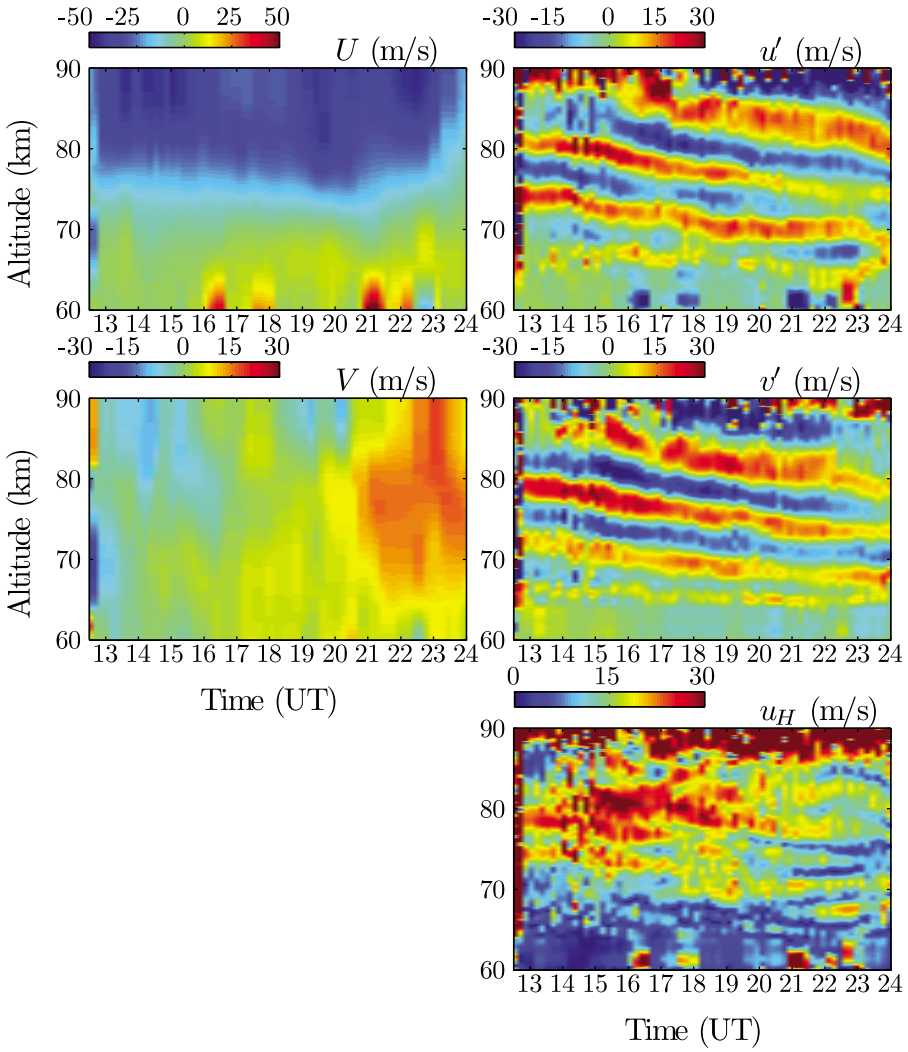

Figure 11. (top left) Background zonal and (bottom left) meridional winds and (right) u', v', and $u'_H = \sqrt{u'^2 + v'^2}$ from 1200 and 2400 UT on 23 April 2008.

weaker, although it still appears to saturate (likely due to the addition of multiple waves which each contribute wind shear to the wavefield, as we discuss in the next section), the acceleration is significantly reduced. This allowed the background wind to relax back to its "normal" state. Since the southward acceleration prior to 2000 UT nearly equals the wind difference before and after 2000 UT, we conclude that this saturating IGW provided nearly all of the acceleration needed for the winds to depart from their normal values prior to 2000 UT. We also note that the background winds after 2000 UT agree well with the HWM quiet time winds, although this is not as conclusive, since the HWM winds cannot account for all of the day-to day variability which occurs in the background winds in the mesosphere.

5.2. Wave Stability

[51] There is a tendency for low-frequency waves (IGWs) to favor dynamical or shear instability over convective (overturning or buoyancy) instability when they dissipate [*Fritts and Rastogi*, 1985; *Fritts and Yuan*, 1989; *Lelong and Dunkerton*, 1998a, 1998b]. This is expected to occur when the local Richardson number for the wavefield is less than 1/4 [e.g., *Gossard and Hooke*, 1975]. The Richardson number depends on both the local Brunt-Väisälä frequency as well as wind shear of the total wavefield. The non-dimensional wave amplitude where dynamical instability is expected based on linear theory for a single wave is [*Fritts and Rastogi*, 1985]

$$a = \frac{1}{2}\sqrt{\zeta^2 + 4\gamma} - \zeta/2 \tag{12}$$

where $\zeta = 4(\omega_{Ir}^2/f^2 - 1)$. The nondimensional wave amplitude corresponds to $|u'_H|/c_I$, where $c_I = \omega_{Ir}/k_H = c_H - U_H$ is the intrinsic horizontal phase speed of the wave, c_H is the ground-based horizontal phase speed, and U_H is the background wind in the direction of wave propagation. Note that equation (12) provides only a guideline for when dynamical instability can occur. In the case of convective instability, it is predicted that this instability occurs when $a = 1$ [*Lindzen*, 1981]; however, numerical simulations show that self interactions for a wave with $a = 0.7$ can create a 2-D instability which then spawns

a 3-D instability that results in turbulence, just as occurs for convective instability [*Fritts et al.*, 2006]. Additionally, equation (12) corresponds only to a single wave and does not imply overall wavefield stability for multiple waves [e.g., *Fritts*, 1984]. For example, multiple waves each contribute wind shear, which can create a wavefield with localized regions where the Richardson number is 1/4, even though the Richardson numbers of the individual waves are greater than 1/4. In the case of convective instability, multiple waves can create steeper potential temperature gradients than for a single wave; in this case, instability occurs where the sum of the nondimensional amplitudes of all waves equals one [*Smith et al.*, 1987].

[52] The nondimensional amplitude of the IGW, a, is plotted in Figure 9 (bottom) along with equation (12). At early times, the non-dimensional amplitude increases with altitude from close to 0 to about 0.75 at 80 km. At these times, the nondimensional amplitudes are very close to the limits for dynamical instability beginning near the altitude where saturation was observed ($z > 70$ km). Note that as ω_{Ir} approaches the inertial frequency (at lower altitudes here), dynamical instability occurs for nondimensional amplitudes much less than 1. This observation, and theoretical work, implies that this IGW saturates from dynamical instability (likely Kelvin-Helmhotz instabilty) and turbulence generation [e.g., *Fritts and Rastogi*, 1985], which has been observed before [e.g., *Fritts et al.*, 1988]. At the later times, as the horizontal wavelength decreases and the intrinsic period decreases, the dynamical instability criteria approaches that for convective instability (i.e., 1). Up to 2000 UT, the altitude where a approaches equation (12) decreases with time, as expected. At 1800–2000 UT, this occurs at 69 km, which agrees with the altitude where the wave begins to saturate (see Figure 9). At times later than 20 UT, the wave's nondimensional amplitude decreases significantly, likely because u'_H decreases, as discussed previously. Even though a is much less than the limit given by equation (12), Figure 7 still indicates that the wave is saturated at these times. The resolution is likely that the multiple waves present in the wavefield result in wave instability, as discussed previously, even though the IGW amplitude may be too small by itself for the instability to occur. The inconsistent hodographs of Figure 7 are also evidence for smaller-scale wave activity.

[53] In section 3.4, we derived turbulence energy dissipation rates from the spectral broadening presumably due to turbulence. This broadening indicated average turbulence dissipation rates of ~30–70 mW/kg, increasing with altitude. These numbers are close to the expectations based on rocket measurements of turbulence energy dissipation rates, which have indicated values of over 100 mW/kg in the summer and about 20 mW/kg in the winter with a strong altitude dependence [*Lübken*, 1997]. We can estimate the contribution of the saturating IGW to the total turbulence by computing the expected energy flux divergence of a gravity wave spectrum with characteristic vertical wavelength of 4–10 km as observed for this wave, assuming that all the energy flux divergence leads to turbulence [i.e., *Fritts and VanZandt*, 1993],

$$\epsilon \approx \frac{NE_0}{18m^\star}\left(\frac{1}{H}-\frac{2}{2H_E}\right) \tag{13}$$

where $H_E \approx 2.3H$ is the energy scale height and E_0 is the total energy per unit mass of an upward propagating spectrum of gravity waves,

$$E_0 = \frac{N^2}{10m^{\star 2}}, \tag{14}$$

and $m^\star$ is the characteristic vertical wave number. These expressions imply total energies of $E_0 \approx 30$–110 m^2/s^2 and turbulence energy dissipation rates of $\epsilon \approx 1.5$–10 mW/kg, or ~5–20% of the total observed energy dissipation rate. This low contribution is not unexpected since smaller-scale, shorter-period waves tend to have larger energy fluxes for a given total wave spectrum energy and are thus more important for momentum and energy transfer [e.g., *Fritts and Vincent*, 1987]. The characteristic $\lambda_z^\star$ that would be required to achieve the measured energy dissipation rate is ~14 km. This seems to be consistent with an analysis of the power spectrum of the vertical velocities (not shown), which can be an estimate of the vertical wave number spectrum for small m [e.g., *Fritts and Hoppe*, 1995; *Hall and Hoppe*, 1997]. Finally, we should note that these methods are very approximate as departures from the canonical gravity wave spectrum would invalidate these results; in addition, interpreting spectral broadening in terms of energy dissipation rates also has uncertainties [e.g., *Gibson-Wilde et al.*, 2000].

5.3. Wave Sources

[54] The IGW we analyzed in this paper propagates extremely slowly in the vertical direction. Its vertical group velocity (see Appendix D for the relevant expressions) is on the order of 0.1–0.13 m/s at ~60 km (where the background winds are nearly zero). Its horizontal group velocity is closer to 10 m/s. These numbers imply that it would take this wave approximately 5–6 days to propagate a vertical distance of ~50 km (up to 60 km from a jet stream altitude of ~10 km) if the intervening winds are assumed negligible. This means the IGW would propagate ~10 km/day vertically and ~1000 km/day horizontally. During this ascent, the wave would propagate a total horizontal distance of 4500–5500 km. If the stratospheric winds along the propagation path were instead northward, the ascent angle would be steeper, and the propagation time and horizontal distance travelled would be shorter. While different scenarios have been investigated by ray-tracing the wave through different background winds (see procedure outlined in Appendix D), it is impossible to identify an exact source region for this IGW without knowing the winds accurately along the wave's entire propagation path. Therefore our goal here is to estimate a possible source region for this IGW given the wind uncertainties. We show below that the winds, which are known up to ~30 km from 12-hourly balloon measurements, could have been oriented mostly perpendicular to the GW propagation direction.

[55] There is only one reasonable source for an IGW with the properties observed here: a geostrophic adjustment of the jet stream. On and around 18 April, the jet stream was located at ~9 km altitude. Following the zero wind assumption, we assume that the wave was excited 5000 ± 500 km northwest of Alaska ~5 days prior to the observations. Using an angle 10° west of north, 5000 km from PFISR is the coast of northern Russia near where the Pechora River enters the

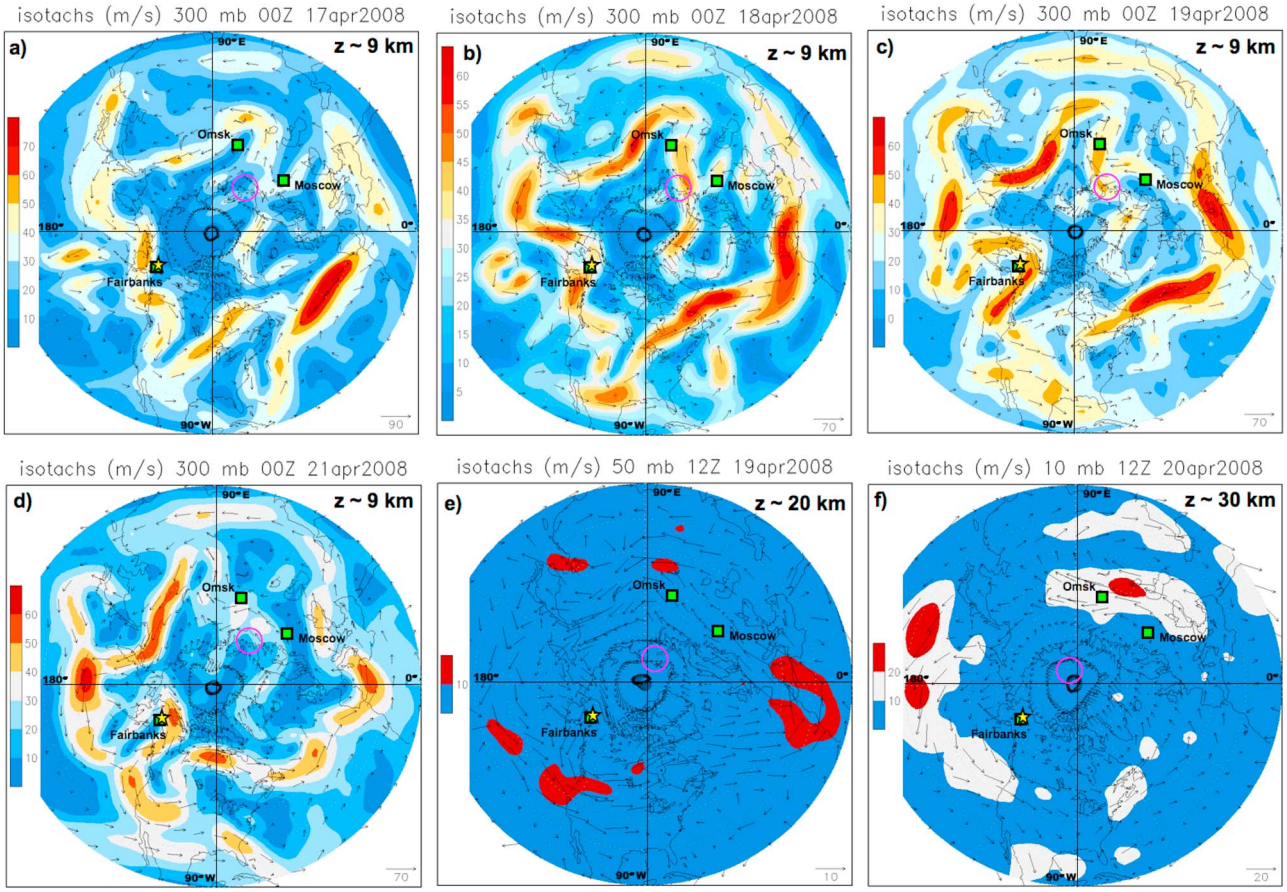

Figure 12. Winds over the Northern Hemisphere in 2008. Arrows are wind vectors; colors are isotachs (wind speed) in m/s. Note that the scales for the vectors and isotach colors change. The yellow star indicates PFISR. Green squares indicate Fairbanks, Alaska; Moscow, Russia (55.8°N, 38.0°E); and Omsk, Russia (54.9°N, 73.4°E). (a) The 300 mb (~9 km) winds at 0000 UT 17 April. Open pink circle is the approximate IGW source location. Winds in the pink circle are toward the northeast (60° east of north) with a magnitude of 19 m/s. (b) As in Figure 12a, except for 0000 UT 18 April. The source location winds are toward the southeast (105° east of north) at 34 m/s. (c) As in Figure 12a, except for 0000 UT 19 April. The source location winds are toward the northeast (55° east of north) with a magnitude of 27 m/s. (d) As in Figure 12a, except for 0000 UT 21 April. The source location winds are toward southeast (105° east of north) at 15 m/s. (e) The 50 mb (z ~ 20 km) winds at 1200 UT 19 April. Open pink circle (diameter of ~1000 km) is the estimated IGW location. Winds in the pink circle are estimated to be toward the east (90° east of north) at 3 m/s. (f) The 10 mb (z ~ 30 km) winds at 1200 UT 20 April. Open pink circle as in Figure 12e. The winds in the pink circle are estimated to be toward the southeast (120° east of north) at 4 m/s.

Pechora Sea, at ~70°N and ~55°E. This is a rough estimate for the source location of this wave because nonzero winds could change this estimated location.

[56] We utilize wind maps over the Northern Hemisphere from the NCEP/DOE Reanalysis (Global R1), available at the NOAA NOMADS Web site [*Rutledge et al.*, 2006]. Tropospheric winds are shown at $z \sim 9$ km (the peak altitude of the jet stream) at 0000 UT in Figures 12a–12d on 17, 18, 19, and 21 April, respectively. The open pink circles show the estimated source location of the IGW, with the diameter indicating the approximate error of the IGW's location given the zero wind assumption. PFISR is indicated by the five-pointed, yellow star. The winds generally flow from west to east at middle and high latitudes, due to the pole-to-equator temperature gradient and the rotation of the Earth. Smaller-scale variations in wind speed and direction are due mainly to local temperature variations and associated storm development and evolution. In Figures 12a–12d, the slower speeds are shown as cooler (blue) colors and the higher speeds as warmer (red) colors (note that the scales change). The narrow areas of higher speeds show the position of the jet stream at this altitude. Note the lack of uniformity in the jet; wind speeds are highest as the air flows around upper-level troughs. For example, at 00 UT 17 April (Figure 12a), an upper trough is located over Omsk (green square in the upper center of Figure 12a). Winds are weak (blue) over the station, with stronger winds moving south to the west of Omsk and moving north to the east. The flow strengthens as the trough moves slowly eastward, and by 19 April (Figure 12c) Omsk is seeing strong southward moving winds at this level. Two days later (Figure 12d) the system has moved well to the east and is weakening, and the strongest winds are on the east side

of the system. Clearly, Figures 12a–12d shows that jet stream adjustments are occurring frequently over the polar region; this implies that IGWs are being excited frequently in a wide variety of locations in the polar region during this time period.

[57] We now focus on the estimated source location for the IGW (open pink circle in Figures 12a–12d). The winds in this region at ~9 km are moving toward the northeast (60° east of north) at 19 m/s at 0000 UT 17 April (Figure 12a). A small-scale system is approaching the area, and by 18 April (Figure 12b) the winds have increased to 34 m/s and veered toward the southeast (105° east of north). The system passes and the winds shift northeastward again (55° east of north) and slow to 27 m/s at 0000 UT 19 April (Figure 12c). The region then remains between systems, and winds steadily weaken over the next two days. By 21 April (Figure 12d), they are moving toward the southeast at 15 m/s.

[58] We estimated above that the IGW was created ~5 days before the PFISR observations. This yields an approximate excitation time of ~1200 UT on 18 April. Therefore we focus on the time period between 0000 UT on 18 April and 0000 UT on 19 April at the source location. At 0000 UT 18 April, the background wind is $(U, V) = (33, -9)$ m/s, while on 19 April, the background wind is $(U, V) = (22, 15)$ m/s. The passing of the small-scale system can be thought of as an external body force because it causes the winds within the pink circle to change as a result of dynamics acting on scales larger than the pink circle. This body force causes the zonal and meridional background winds to change by $(\Delta U, \Delta V) = (-11, 24)$ m/s over this time period. This body force has northward and westward components. We consider here only the northward component, which will excite primarily northward and southward propagating IGWs. (The westward component will excite negligible northward IGWs [e.g., *Vadas et al.*, 2003].) Using 12-hourly balloon soundings taken at Narjan-Mar (Russia, 67.6°N and 53.0°E), which is within the pink circle, we find that the change in the meridional winds occurs in 12 h or less (not shown). Therefore the minimum northward acceleration experienced by the fluid in this region is ~2 m/s/hr. From Figures 12b–12c, we see that the total horizontal extent of the body force is ~500 km. Using the balloon soundings, we estimate the depth of this northward body force to be ~5 km. (S. L. Vadas, submitted manuscript, 2010b) model this body force with a total duration of 6 h and find that it excites a spectrum of IGWs with λ_H of several hundred to many thousands of km. In particular, those waves that are excited with $\lambda_H \sim 700$–1000 km and $\lambda_z \sim 5$–7 km have intrinsic horizontal phase speeds of $c_{IH} = 20$–30 m/s. Because the jet stream adjustment created a northward wind component of ~15 m/s by 0000 UT on 19 April, and a meridionally propagating GW's ground-based phase speed is $c_y = c_{Iy} - V$, the northward propagating IGWs with $c_{IH} = 20$–30 m/s have ground-based phase speeds of $c_y = 5$–15 m/s. Thus the parameters of these IGWs are consistent with the IGWs observed above PFISR.

[59] Again assuming that the IGW observed at PFISR was excited at ~1200 UT on 18 April, we now estimate its location at later times. One (two) day(s) later, we expect this IGW to be located at $z \sim 20$ (~30) km, at a horizontal distance of ~1000 (~2000) km from its excitation location. Figure 12e shows the winds near 20 km at 1200 UT on 19 April. The open pink circle is the estimated location of the wave at this time and altitude assuming that it travels in a straight line. Winds in the vicinity of the wave are moving toward the east at 3 m/s. Because the IGW is propagating approximately perpendicular to the background wind, it will not be affected by this wind. The 30 km winds at 1200 UT 20 April are shown in Figure 12f, and the open circle is the estimated wave location as in Figure 12e. Winds near the wave at this altitude and time are moving toward the southeast (120° east of north) at 4 m/s. This wind is therefore nearly perpendicular to the direction of propagation; as before, it will not affect the wave. At both of these altitudes, the wave is moving through light winds near the pole, well away from the more active regions of stronger winds at lower latitudes. Stronger northward winds might have resulted in the IGW reaching a critical level in the stratosphere from tides, planetary waves, and QBOs.

[60] Although our observations might initially suggest a single IGW, we have shown here that we are instead likely seeing a packet of IGWs generated by geostrophic adjustment of the jet stream near the tropopause. The observation that the ground-relative period decreases with altitude is consistent with this scenario. Consider that this IGW is propagating at least 100 times faster in the horizontal direction than in the vertical. It then becomes apparent that the wave will propagate out of the field-of-view of the radar (at most ~30 km horizontally) before traveling a fraction of its vertical wavelength in the vertical direction. Thus each ~10 km bin in altitude represents an observation of a different wave, from what appears to be an extremely coherent source (as evidenced by the early hodographs in Figure 7, for example). For such a source, one would expect waves to be generated as dictated by the following relationship:

$$\omega_r^2 = N^2 \sin^2\theta + f^2 \cos^2\theta \tag{15}$$

where θ is the propagation angle (from the horizontal) and the expression neglects the winds at the source. For the wave in question, the ratio of the vertical to horizontal wave number indicates that θ must be extremely small, ~0.15°. In this regime, one can make a small-angle approximation and we find,

$$\tau \approx \frac{2\pi}{f\left[1 + \frac{1}{2}\theta^2 N^2/f^2\right]}. \tag{16}$$

This expression indicates that the observed ground-relative period will decrease with altitude for a single-location observer as waves are launched with decreasing values of θ. A simple evaluation of this expressions indicates that one would expect the observed period to decrease by approximately 1.5–2 h from 60 to 90 km from a single source, which is similar to what was observed and assumed in the analysis presented in this paper.

[61] We note that the coherency of the oscillations with altitude for a single-location observer is also seen in the model results of a geostrophic adjustment process (S. L. Vadas, submitted manuscript, 2010b), even though this altitude range spans many IGWs with somewhat different properties, as discussed above. Additionally, this model predicted horizontal wind velocities of ~1.3 m/s at $z = 61$ km for these IGWs. This value agrees well with the measured values at this altitude (Figure 7). Thus the model results of IGWs excited by a jet stream adjustment (modeled as a body force) are consistent with our observations.

[62] Finally, we point out that the model results do not include wave saturation. However, they show variations in altitude of u' and v' that are not always exponential in nature. This variation is due entirely to amplitude variations of the IGWs within the excited spectrum, as well as to the fact that we are observing many IGWs over a large altitude range. Therefore one must be careful not to interpret the constancy (or decrease) of u' and v' with altitude as a definitive indication of wave saturation when the altitude range encompasses many different low-frequency waves. In this paper, we used the constancy of u' and v' with altitude as a possible clue of wave saturation. Then, we calculated the nondimensional wave amplitudes, which showed further evidence that the IGWs were saturating.

6. Conclusion

[63] In this paper we have explored in detail a case study of an inertia-gravity wave observed continuously for over ~12 h in the mesosphere over Alaska. These observations were afforded by very sensitive measurements of the *D* region ionosphere with the Poker Flat Incoherent Scatter Radar. Because of PFISR's rapid beam-steering capability, we were able to obtain line-of-sight ion velocities in seven different look directions, from which we were able to derive vector winds in addition to vertical velocities, Doppler spectra, and calibrated reflectivity. The analysis of the *D* region, collisional spectra included deriving Doppler motions, signal strength (calibrated to N_e), and spectral widths. The spectral widths were interpreted in terms of IS theory coupled to turbulent motions expected in this environment.

[64] The IGW properties were determined using polarization and hodograph techniques, although there was some uncertainty resulting from the short vertical wavelengths (5–10 km, increasing with altitude) and the changing wave properties in time. We derived expressions relating the polarization of the horizontal wind perturbations to each other, to the vertical winds, and to the spectral width perturbations (for incoherent scatter, related to temperature and neutral density perturbations). Evidence was presented that the wave was propagating predominantly southward, with a ground-based period of ~10.5 h. The period was observed to decrease in altitude, consistent with the expectations of a source region generating waves with very low vertical speeds. The horizontal wavelengths of this wave were observed to decrease in time from ~1600 km to ~700 km over the observation window. This decrease was hypothesized to be a result of both source characteristics and gradients in the background meridional winds, which could be generated by local body forcing due to wave dissipation.

[65] Interesting trends were observed in the background winds and in the wave amplitudes. The background winds were observed to be southward for the first ~8 h of the observations, approximately 10–20 m/s southward of the HWM winds. The winds then relaxed to the north by ~10–20 m/s. In conjunction with this relaxation, the wave amplitudes were observed to decrease by roughly the same amount. Simultaneously, the wave was shown to be saturated: its scaled (to account for the exponential atmosphere) amplitude was observed to decrease in altitude above some point. The observations of wind acceleration and saturation are consistent with our expectations for acceleration of the background flow by a saturated/dissipating wave. A stability analysis seems to confirm that the wave had reached or was very close to the condition for dynamical instability. Because of the very small vertical phase speeds of this wave, other factors may have contributed to the variations of the wave amplitude with altitude and time: namely, amplitude variations in the wave spectrum generated by the excitation process. While we cannot rule this possibility out, several independent factors point to wave saturation and dissipation.

[66] Finally, while ray tracing of this wave was not possible due to uncertainties of the winds along the propagation path, the wave was hypothesized to have been generated by geostrophic adjustment of the jet stream. Given its propagation direction and speed, a possible source was jet stream adjustment in northern Russia (~5000 km away) approximately 5 days before the observations at PFISR; indeed, the winds along the propagation path seem to be favorable for the wave to reach mesospheric altitudes over central Alaska with the observed characteristics.

Appendix A: Outlier Removal

[67] The real and imaginary parts of a complex signal, denoted by x_r and x_i, respectively, are both described by the zero-mean Gaussian probability distribution function (pdf) with standard deviation σ,

$$\frac{1}{\sqrt{2\pi\sigma^2}}\exp\left(-\frac{x_{r,i}^2}{2\sigma^2}\right). \tag{A1}$$

The probability that $x_{r,i} > \beta$, the so-called right-tail probability, is given by one minus the cumulative distribution function,

$$\mathrm{prob}\left(x_{r,i} > \beta\right) = \frac{1}{2}\mathrm{erfc}\left(\frac{\beta}{\sqrt{2\sigma^2}}\right) \tag{A2}$$

where erfc denotes the complementary error function. The probability that at least one of N independent samples is greater than β is therefore

$$1 - \left[1 - \frac{1}{2}\,\mathrm{erfc}\left(\frac{\beta}{\sqrt{2\sigma^2}}\right)\right]^N. \tag{A3}$$

Setting equation (A3) equal to $\frac{1}{x}$, if no outliers are present, there is a $\frac{100}{x}$% chance that one of N points is greater than the solution,

$$\beta = \sqrt{2\sigma^2}\,\mathrm{erfcinv}\left\{2\left[1 - \left(1 - \frac{1}{x}\right)^{1/N}\right]\right\}. \tag{A4}$$

Suppose we are given N data points, and we wish to determine which, if any, are outliers. (By an outlier, we mean a data point belonging to another statistical distribution.) If we use $x = 2$ and decide that all points greater than β in equation (A4) are outliers, there will be a 50% chance that we will discard a data point.

[68] In the preceding analysis, we assumed that we are able to determine the variance, σ^2. The variance is the mean of $x_{r,i}^2$ and is usually estimated from the sample mean. But in the presence of outliers, the sample mean will not be a good estimate of the true pdf mean, especially in light of the fact

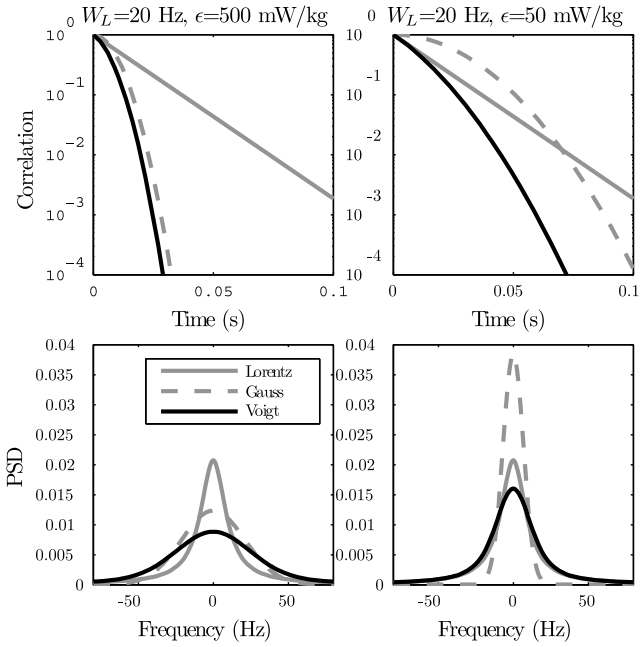

Figure B1. Examples of expected power spectral density due to *D* region incoherent scatter broadened by turbulence. (top) Correlation functions for the Gaussian (dashed gray), the Lorentzian (solid gray), and the Voigt (black) line shapes. (bottom) Corresponding power spectra. (left) The case of strong turbulence (ϵ = 500 mW/kg) and a fairly narrow incoherent scatter spectral width of W_L = 20 Hz. (right) Same, except for weaker turbulence, ϵ = 50 mW/kg.

that we are intending to use this variance to gauge outliers. However, we know that the pdf for $y = x_r^2 + x_i^2$ is the Chi-squared distribution,

$$\frac{1}{2\sigma^2}\exp\left(-\frac{y}{2\sigma^2}\right). \tag{A5}$$

The right-tail probability of this pdf is

$$\exp\left(-\frac{y}{2\sigma^2}\right). \tag{A6}$$

Setting this equal to $\frac{1}{2}$ and solving for y gives the median

$$b = 2\sigma^2 \ln 2. \tag{A7}$$

Estimation of the median can be done by simply taking the central point, which is robust even when outliers are present. Therefore we proceed by estimating the median of y and using equation (A7) to solve for an estimate of σ^2 that is robust to outliers; we can then apply equation (A4) to set the outlier threshold.

Appendix B: Voigt Function for Incoherent Scatter

[69] The Voigt profile is a well-known spectroscopic line shape [e.g., *Thorne et al.*, 1999] describing a Lorentzian process that is Doppler broadened by a Gaussian process. This describes well *D* region incoherent scatter, wherein the normal Lorentzian line shape can be affected by Doppler motions associated with turbulence. The Voigt function then represents the convolution of the Gaussian power spectral shape with the Lorentzian power spectral shape shape of the form

$$V(\nu;\sigma,\gamma,\delta\nu) = G(\nu;\sigma,\delta\nu) \star L(\nu;\gamma,\delta\nu) \tag{B1}$$

$$G(\nu;\sigma,\delta\nu) = \frac{1}{\sigma\sqrt{2\pi}}\exp\left[-\frac{\nu^2}{2\sigma^2}\right] \tag{B2}$$

$$L(\nu;\gamma,\delta\nu) = \frac{\gamma}{\pi\left[(\nu-\delta\nu)^2+\gamma^2\right]} \tag{B3}$$

where the star symbol represents the convolution operator, $W_G = 2\sigma\sqrt{2\ln 2}$ is the full-width at half-maximum (FWHM) of the Gaussian, $W_L = 2\gamma$ is the FWHM of the Lorentzian, ν is frequency, and $\delta\nu$ is a Doppler shift. The analytic solution to the convolution involves the error function, but for the case of incoherent scatter, the time domain representation is extremely useful. This corresponds to

$$V(\tau;\sigma,\gamma,\delta\nu) = G(\tau;\sigma,\delta f)L(\tau;\gamma,\delta\nu) \tag{B4}$$

$$G(\tau;\sigma) = \exp\left[-2\pi^2\tau^2\sigma^2\right] \tag{B5}$$

$$L(\tau;\gamma,\delta\nu) = \exp[2\pi j\tau\delta\nu - W_L\pi\tau]. \tag{B6}$$

For the purposes of IS, the spectrum can then be represented by three parameters (W_G, W_L, $\delta\nu$) along with possibly an amplitude and noise floor level. This representation can be understood as turbulence slightly reducing the intrinsic correlations of the medium, thus broadening the spectrum somewhat.

[70] In Figure B1 we show expected spectral shapes for a given IS Lorentzian width (W_L = 20 Hz) and for two turbulence strengths: strong (left) and weak (right). The Lorentzian width corresponds to the expected width for PFISR at ~70–75 km. The turbulence energy dissipation rate can be related to the velocity variance of the scatterers by [*Weinstock*, 1981; *Hocking*, 1996]

$$\epsilon \approx 9.8\sigma_v^2 \text{ mW/kg}. \tag{B7}$$

The strong turbulence case is dominated by the Gaussian (turbulent) contribution; the weaker turbulence case is dominated by the Lorentzian except that the peak of the distribution is flattened out by the turbulent component.

Appendix C: Gravity Wave Phase Relationships

C1. Gravity Wave Perturbation Analysis

[71] We define mean and perturbation temperature, pressure, and mass density, $T = \bar{T} + T'$, $p = \bar{p} + p'$, and $\rho = \bar{\rho} + \rho'$, respectively, and normalized perturbations as $\tilde{T} = T'/\bar{T}$, $\tilde{p} = p'/\bar{p}$, and $\tilde{\rho} = \rho'/\bar{\rho}$, where $p = \rho RT$. Here, the overlines denote the mean values and primes denote the perturbation quantities. These perturbations vary sinusoidally in time and space as $\exp(i\mathbf{k}\cdot\mathbf{x} - i\omega_r t)$. In the following, we will use the Boussinesq approximation [see *Vadas and Fritts*, 2001, equations (2.1)–(2.5)], valid for $m^2 \gg 1/4H^2$ or $\lambda_z \ll 4\pi H$,

where $H = R\bar{T}/g$ is the (isothermal) scale height. For a more rigorous analysis which includes full compressibility, we refer the reader to (S. L. Vadas, submitted manuscript, 2010a).

[72] Temperature perturbations can be derived from the potential temperature, which is defined as [e.g., *Holton*, 1992]

$$\theta = T\left(\frac{p_0}{p}\right)^{R/C_P} \tag{C1}$$

where $R/C_P = (\gamma - 1)/\gamma$, p_0 is the pressure at sea level, R is the gas constant, $\gamma = C_P/C_V$ is the ratio of specific heats, and C_P and C_V are the mean specific heats at constant pressure and volume, respectively. From this expression, the following perturbation relationship can be derived:

$$\tilde{\theta} = \frac{\tilde{p}}{\gamma R\bar{T}} - \tilde{\rho} = \tilde{T} - \frac{\tilde{p}}{C_P\bar{T}}, \tag{C2}$$

where $\tilde{\theta} = \theta'/\bar{\theta}$. Potential temperature perturbations are related to vertical velocity perturbations as

$$\tilde{\theta} = -i\frac{N^2}{\omega_{Ir}g}\tilde{w} \tag{C3}$$

which are in turn related to pressure perturbations as

$$\tilde{w} = -\frac{m\omega_{Ir}}{N^2 - \omega_{Ir}^2}\tilde{p}. \tag{C4}$$

The temperature perturbation is then given by

$$\tilde{T} = \frac{1}{g}\frac{im}{(1 - \omega_{Ir}^2/N^2)}\tilde{p}. \tag{C5}$$

Making the assumption that $N^2 \gg \omega_{Ir}^2$, suitable for long-period inertia-gravity waves,

$$\tilde{T} = \frac{im}{g}\tilde{p}. \tag{C6}$$

The pressure perturbation is also related to the zonal and meridional wind perturbations by

$$\tilde{p} = \frac{\omega_{Ir}^2 - f^2}{\omega_{Ir}k + if\ell}\tilde{u} = \frac{\omega_{Ir}^2 - f^2}{\omega_{Ir}\ell - ifk}\tilde{v}. \tag{C7}$$

C2. Vertical Velocity Perturbations

[73] Vertical and horizontal winds are related by equations (C4) and (C7), which may be written as

$$\tilde{w} = -\frac{m\omega_{Ir}}{N^2}\frac{\omega_{Ir}^2 - f^2}{\omega_{Ir}^2k^2 + f^2\ell^2}(\omega_{Ir}k - if\ell)\tilde{u} \tag{C8}$$

$$\tilde{w} = -\frac{m\omega_{Ir}}{N^2}\frac{\omega_{Ir}^2 - f^2}{\omega_{Ir}^2\ell^2 + f^2k^2}(\omega_{Ir}\ell + ifk)\tilde{v} \tag{C9}$$

assuming that $N^2 \gg \omega_{Ir}^2$ (and that $m^2 \gg 1/4H^2$). These equations imply that for a zonally, upward propagating wave ($\ell \to 0, m < 0$), $\tilde{w}$ and $\tilde{u}$ will be in phase (180° out of phase) for eastward (westward) propagating waves. On the other hand, $\tilde{w}$ and $\tilde{v}$ will be 90° out of phase, with $\tilde{w}$ lagging (leading) for eastward (westward) propagating waves. For a meridionally, upward propagating wave ($k \to 0, m < 0$), $\tilde{w}$ and $\tilde{u}$ will be out of phase by 90°, with $\tilde{w}$ leading (lagging) for northward (southward) propagating waves. In this case, $\tilde{w}$ and $\tilde{v}$ would be in phase (180° out of phase) for northward (southward) propagating waves. For more general angles, we can further write

$$\begin{aligned}\tan\phi_{\tilde{w},\tilde{u}} &= -\frac{f}{\omega_{Ir}}\tan\alpha \\ \tan\phi_{\tilde{w},\tilde{v}} &= \frac{f}{\omega_{Ir}}\frac{1}{\tan\alpha}\end{aligned} \tag{C10}$$

where $k = k_H\cos\alpha$ and $\ell = k_H\sin\alpha$, $k_H = \sqrt{k^2 + \ell^2}$ is the horizontal wave number, and α is the propagation direction, positive north of east. Additionally, $\phi_{\tilde{w},\tilde{u}}$ and $\phi_{\tilde{w},\tilde{v}}$ are the phase shifts between $\tilde{w}$ and $\tilde{u}$ and between $\tilde{w}$ and $\tilde{v}$, respectively. From measurements of $\phi_{\tilde{w},\tilde{u}}$ and $\phi_{\tilde{w},\tilde{v}}$ these expressions allow us to calculate the direction of propagation α along with the ratio of the intrinsic to inertial frequencies. The propagation direction may be calculated (with 180° ambiguity) from

$$\tan^2\alpha = -\frac{\tan\phi_{\tilde{w},\tilde{u}}}{\tan\phi_{\tilde{w},\tilde{v}}}. \tag{C11}$$

The sign of the propagation angle can be resolved by examination of equations (C8) and (C9). Defining $v = u'\cos\alpha + v'\sin\alpha$ as the horizontal wave velocity perturbation in the direction of propagation, we find that

$$\tilde{w} = -\tilde{v}\frac{m}{k_H}\frac{\left(\omega_{Ir}^2 - f^2\right)}{N^2}. \tag{C12}$$

C3. Incoherent Scatter Spectral Width Perturbations

[74] The half-power half-width for the Lorentzian *D* region incoherent scatter spectra neglecting the presence of negative ions [e.g., *Mathews*, 1978; *Raizada et al.*, 2008], dust [e.g., *Cho et al.*, 1998], and other charged particles, and assuming thermal equilibrium between ions, electrons, and neutrals, is given by [e.g., *Dougherty and Farley*, 1963]

$$\gamma \approx \frac{16\pi k_B T}{\lambda_R^2 m_i \nu_{in}}. \tag{C13}$$

The spectral width may be written as

$$\gamma \propto \frac{T}{\rho} \tag{C14}$$

since the collision frequency is proportional to the neutral density [e.g., *Banks and Kockarts*, 1973]. Spectral width perturbations associated with the passage of a gravity wave will be due to perturbations in temperature and neutral density so that

$$\tilde{\gamma} = \frac{\gamma'}{\bar{\gamma}} = \tilde{T} - \tilde{\rho} = 2\tilde{T} - \frac{\tilde{p}}{R\bar{T}}. \tag{C15}$$

[75] In the Boussinesq approximation, the pressure term is negligible because $R\bar{T} = gH$. Then, the spectral width perturbation is simply (using equation (C6)):

$$\tilde{\gamma} \approx 2\tilde{T} \approx \frac{2im}{g}\tilde{p}. \tag{C16}$$

Using equation (C7), $\tilde{\gamma}$ is related to the horizontal wind perturbations via

$$\tilde{\gamma} = \frac{2m}{g}\,\frac{\omega_{Ir}^2 - f^2}{\omega_{Ir}^2 k^2 + f^2\ell^2}(i\omega_{Ir}k + f\ell)\tilde{u} \tag{C17}$$

$$= \frac{2m}{g}\,\frac{\omega_{Ir}^2 - f^2}{\omega_{Ir}^2 \ell^2 + f^2 k^2}(i\omega_{Ir}\ell - fk)\tilde{v}. \tag{C18}$$

[76] Equations (C17) and (C18) imply that for a zonally propagating wave ($\ell \to 0$), there would be a 90° phase shift between $\tilde{\gamma}$ and $\tilde{u}$, with $\tilde{\gamma}$ leading $\tilde{u}$ in altitude/time for a wave propagating eastward ($k > 0$) and upward ($m < 0$) and $\tilde{\gamma}$ lagging $\tilde{u}$ as a function of altitude for a wave propagating westward ($k < 0$) and upward ($m < 0$). Here $\tilde{\gamma}$ and $\tilde{v}$ would be in phase ($k > 0$) and out of phase ($k < 0$) for these two cases ($m < 0$). For a meridionally propagating wave ($k \to 0$) with $m < 0$, $\tilde{\gamma}$ and $\tilde{u}$ would be out of phase for $\ell > 0$ (northward) and in phase for $\ell < 0$ (southward). For $\ell > 0$ ($\ell < 0$), $\tilde{\gamma}$ would lead (lag) $\tilde{v}$ by 90°. For more general angles, we can proceed as in section C2 to determine the propagation direction for the phase offsets.

Appendix D: Derivatives for Ray Tracing

[77] For ray tracing, we use the Boussinesq dispersion relation given by [e.g., *Fritts and Alexander*, 2003]

$$\omega_{Ir}^2 = \frac{N^2 k_H^2 + f^2 m^2}{k_H^2 + m^2}. \tag{D1}$$

The group velocities from this dispersion relation can be written as

$$c_{gz} = \frac{\partial\omega_{Ir}}{\partial m} = -\frac{m\left(\omega_{Ir}^2 - f^2\right)}{\omega_{Ir}\left(k_H^2 + m^2\right)} \tag{D2}$$

$$c_{gx} = \frac{\partial\omega_{Ir}}{\partial k} = \frac{km^2(N^2 - f^2)}{\omega_{Ir}\left(k_H^2 + m^2\right)^2} \tag{D3}$$

$$c_{gy} = \frac{\partial\omega_{Ir}}{\partial \ell} = \frac{\ell m^2(N^2 - f^2)}{\omega_{Ir}\left(k_H^2 + m^2\right)^2}. \tag{D4}$$

The ray trace equations are then given by [e.g., *Lighthill*, 1978; *Vadas and Fritts*, 2005]

$$\frac{dx_i}{dt} = U_i + c_{gi} \tag{D5}$$

$$\frac{dk_i}{dt} = -k_j\frac{\partial U_j}{\partial x_i} - \frac{\partial\omega_{Ir}}{\partial x_i} \tag{D6}$$

where the index i refers to Cartesian position (x, y, z) and repeated indices imply summation. The last term of equation (D6) is given by

$$\frac{\partial\omega_{Ir}}{\partial x_i} = \frac{N}{\omega_{Ir}}\,\frac{k_H^2}{k_H^2 + m^2}\,\frac{\partial N}{\partial x_i} + \frac{f}{\omega_{Ir}}\,\frac{m^2}{k_H^2 + m^2}\,\frac{\partial f}{\partial x_i}. \tag{D7}$$

In our ray tracing, we ignore variations of f with z (i.e., consider only the y variations).

[78] **Acknowledgments.** PFISR was developed under NSF cooperative agreement ATM-0121483, and the data collection and analysis was supported under NSF cooperative agreement ATM-0608577. Work at SRI International was sponsored by NSF under grant ATM-0836142. Work at NWRA/CoRA was sponsored by NSF under grant ATM-0836195. NCEP/DOE Reanalysis (Global R1) data was obtained from the NOAA NOMADS Web site (http://nomads.ncdc.noaa.gov). The authors would like to thank D. C. Fritts and J. L. Chau for helpful discussions.

References

Andrews, D. G., J. R. Holton, and C. B. Leovy (1987), *Middle Atmosphere Dynamics*, Academic, Orlando, Fla.

Banks, P. M., and G. Kockarts (1973), *Aeronomy*, Academic, New York.

Barat, J., and C. Cot (1992), Wind shear rotary spectra in the atmosphere, *Geophys. Res. Lett.*, *19*, 103–106.

Chau, J. L., and E. Kudeki (2006), First *E*- and *D*-region incoherent scatter spectra observed over Jicamarca, *Ann. Geophys.*, *24*, 1295–1303.

Cho, J. Y. N. (1995), Inertio-gravity wave parameter estimation from cross-spectral analysis, *J. Geophys. Res.*, *100*, 18,727–18,738.

Cho, J. Y. N., M. P. Sulzer, and M. C. Kelley (1998), Meteoric dust effects on *D*-region incoherent scatter radar spectra, *J. Atmos. Sol. Terr. Phys.*, *60*, 349–357.

Collins, R. L., and R. W. Smith (2004), Evidence of damping and overturning of gravity waves in the Arctic mesosphere: Na lidar and OH temperature observations, *J. Atmos. Sol. Terr. Phys.*, *66*, 867–879.

Collins, R. L., D. C. Senft, and C. S. Gardner (1992), Observations of a 12 H wave in the mesopause region at the South Pole, *Geophys. Res. Lett.*, *19*, 57–60.

Collins, R. L., T. Xin, and C. S. Gardner (1996), Gravity wave activity in the upper mesophere over Urbana, Illinois: lidar observations and analysis of gravity wave propagation models, *J. Atmos. Sol. Terr. Phys.*, *58*, 1905–1926.

Collis, P. N., and M. T. Rietveld (1998), Mesospheric observations with the EISCAT UHF radar during polar cap absorption events: 3. Comparison with simultaneous EISCAT VHF measurements, *Ann. Geophys.*, *16*, 1355–1366.

Cornish, C. R., and M. F. Larsen (1989), Observations of low-frequency inertia-gravity waves in the lower stratosphere over Arecibo, *J. Atmos. Sci.*, *46*, 2428–2439.

Cot, C., and J. Barat (1986), Wave-turbulence interaction in the stratosphere: A case study, *J. Geophys. Res.*, *91*, 2749–2756.

Dougherty, J. P., and D. T. Farley (1963), A theory of incoherent scattering of radio waves by a plasma: 3. Scattering in a partly ionized gas, *J. Geophys. Res.*, *68*, 5473–5486.

Drob, D. P., et al. (2008), An empirical model of the Earth's horizontal wind fields: HWM07, *J. Geophys. Res.*, *113*, A12304, doi:10.1029/2008JA013668.

Fritts, D. C. (1984), Gravity wave saturation in the middle atmosphere - A review of theory and observations, *Rev. Geophys.*, *22*, 275–308.

Fritts, D. C., and M. J. Alexander (2003), Gravity wave dynamics and effects in the middle atmosphere, *Rev. Geophys.*, *41*(1), 1003, doi:10.1029/2001RG000106.

Fritts, D. C., and U. Hoppe (1995), High-resolution measurements of vertical velocity with the European incoherent scatter VHF radar 2. Spectral observations and model comparisons, *J. Geophys. Res.*, *100*, 16,827–16,838.

Fritts, D. C., and Z. Luo (1992), Gravity wave excitation by geostrophic adjustment of the jet stream, part 1: Two-dimensional forcing, *J. Atmos. Sci.*, *49*, 681–697.

Fritts, D. C., and P. K. Rastogi (1985), Convective and dynamical instabilities due to gravity wave motions in the lower and middle atmosphere: Theory and observations, *Radio Sci.*, *20*, 1247–1277.

Fritts, D. C., and T. E. VanZandt (1993), Spectral estimates of gravity wave energy and momentum fluxes. Part 1: Energy dissipation, acceleration, and constraints, *J. Atmos. Sci.*, *50*, 3685–3694.

Fritts, D. C., and R. A. Vincent (1987), Mesospheric momentum flux studies at Adelaide, Australia - Observations and a gravity wave-tidal interaction model, *J. Atmos. Sci.*, *44*, 605–619.

Fritts, D. C., and L. Yuan (1989), Stability analysis of inertio-gravity wave structure in the middle atmosphere, *J. Atmos. Sci.*, *46*, 1738–1745.

Fritts, D. C., S. A. Smith, B. B. Balsley, and C. R. Philbrick (1988), Evidence of gravity wave saturation and local turbulence production in the summer mesosphere and lower thermosphere during the STATE experiment, *J. Geophys. Res.*, *93*, 7015–7025.

Fritts, D. C., S. L. Vadas, K. Wan, and J. A. Werner (2006), Mean and variable forcing of the middle atmosphere by gravity waves, *J. Atmos. Sol. Terr. Phys.*, *68*, 247–265.

Gavrilov, N. M., S. Fukao, T. Nakamura, T. Tsuda, M. D. Yamanaka, and M. Yamamoto (1996), Statistical analysis of gravity waves observed with the middle and upper atmosphere radar in the middle atmosphere: 1. Method and general characteristics, *J. Geophys. Res.*, *101*, 29,511–29,522, doi:10.1029/96JD01447.

Gibson-Wilde, D., J. Werne, D. Fritts, and R. Hill (2000), Direct numerical simulation of VHF radar measurements of turbulence in the mesosphere, *Radio Sci.*, *35*, 783–798, doi:10.1029/1999RS002269.

Gossard, E., and W. Hooke (1975), *Waves in the Atmosphere*, Elsevier, New York.

Guest, F. M., M. J. Reeder, C. J. Marks, and D. J. Karoly (2000), Intertia-gravity waves observed in the lower stratosphere over Macquarie Island, *J. Atmos. Sci.*, *57*, 737–752.

Hall, C. M., and U. Hoppe (1997), Characteristic vertical wavenumbers for the polar mesosphere, *Geophys. Res. Lett.*, *24*, 837–840, doi:10.1029/97GL00805.

Heinselman, C. J., and M. J. Nicolls (2008), A Bayesian approach to electric field and *E*-region neutral wind estimation with the Poker Flat Advanced Modular Incoherent Scatter Radar, *Radio Sci.*, *43*, RS5013, doi:10.1029/2007RS003805.

Hernandez, G., R. W. Smith, and J. F. Conner (1992), Neutral wind and temperature in the upper mesosphere above South Pole, Antarctica, *Geophys. Res. Lett.*, *19*, 53–56.

Hill, R. J., and S. A. Bowhill (1977), Collision frequencies for use in the continuum momentum equations applied to the lower ionosphere, *J. Atmos. Terr. Phys.*, *39*, 803–811.

Hines, C. O. (1960), Internal atmospheric gravity waves at ionospheric heights, *Can. J. Phys.*, *38*, 1441–1481.

Hines, C. O. (1989), Tropopausal mountain waves over Arecibo: A case study, *J. Atmos. Sci.*, *46*, 476–488.

Hocking, W. K. (1985), Measurement of turbulent energy dissipation rates in the middle atmosphere by radar techniques: A review, *Radio Sci.*, *20*(6), 1403–1422.

Hocking, W. K. (1996), An assessment of the capabilities and limitations of radars in measurements of upper atmosphere turbulence, *Adv. Space Res.*, *17*(11), 37–47.

Holton, J. R. (1992), *An Introduction to Dynamic Meteorology*, 3rd ed., Academic, New York.

Hu, X., A. Z. Liu, C. S. Gardner, and G. R. Swenson (2002), Characteristics of quasi-monochromatic gravity waves observed with Na lidar in the mesopause region at Starfire Optical Range, NM, *Geophys. Res. Lett.*, *29*(24), 2169, doi:10.1029/2002GL014975.

Janches, D., D. C. Fritts, M. J. Nicolls, and C. J. Heinselman (2009), Observations of *D*-region structure and atmospheric tides with PFISR during active aurora, *J. Atmos. Sol. Terr. Phys.*, *71*, 688–696, doi:10.1016/j.jastp.2008.08.015.

Johnson, R. M., and J. G. Luhmann (1993), Poker Flat MST radar observations of high latitude neutral winds at the mesopause during and after solar proton events, *J. Atmos. Sol. Terr. Phys.*, *55*, 1203–1218.

Lelong, M., and T. J. Dunkerton (1998a), Inertia-gravity wave breaking in three dimensions. Part I: Convectively stable waves, *J. Atmos. Sci.*, *55*, 2473–2488.

Lelong, M., and T. J. Dunkerton (1998b), Inertia-gravity wave breaking in three dimensions. Part II: Convectively unstable waves, *J. Atmos. Sci.*, *55*, 2489–2501.

Li, T., C.-Y. She, H.-L. Liu, T. Leblanc, and I. S. McDermid (2007), Sodium lidar - observed strong inertia-gravity wave activities in the mesopause region over Fort Collins, Colorado (41°N, 105°W), *J. Geophys. Res.*, *112*, D22104, doi:10.1029/2007JD008681.

Lighthill, J. (1978), *Waves in Fluids*, Cambridge Univ. Press, New York.

Lindzen, R. S. (1981), Turbulence and stress owing to gravity wave and tidal breakdown, *J. Geophys. Res.*, *86*, 9707–9714.

Liu, H.-L., and J. W. Meriwether (2004), Analysis of a temperature inversion event in the lower mesosphere, *J. Geophys. Res.*, *109*, D02S07, doi:10.1029/2002JD003026.

Lübken, F. (1997), Seasonal variation of turbulent energy dissipation rates at high latitudes as determined by in situ measurements of neutral density fluctuations, *J. Geophys. Res.*, *102*, 13,441–13,456.

Luo, Z., and D. C. Fritts (1993), Gravity wave excitation by geostrophic adjustment of the jet stream, part ii: Three-dimensional forcing, *J. Atmos. Sci.*, *50*, 104–115.

Mathews, J. D. (1978), The effects of negative ions on collision-dominated Thomson scattering, *J. Geophys. Res.*, *83*, 505–512.

Mathews, J. D. (1986), Incoherent scatter radar probing of the 60–100 km atmosphere and ionosphere, *IEEE Trans. Geosci. Remote Sens.*, *24*(5), 765–776.

Mitchell, N. J., L. Thomas, and I. T. Prichard (1994), Gravity waves in the stratosphere and troposphere observed by lidar and MST radar, *J. Atmos. Terr. Phys.*, *56*, 939–947.

Murakoa, Y., T. Sugiyama, K. Kawahira, T. Sato, and T. Tsuda (1988), Cause of a monochromatic inertia-gravity wave breaking observed by the Mu radar, *Geophys. Res. Lett.*, *15*, 1349–1352, doi:10.1029/GL015i012p01349.

Muraoka, Y., K. Kawahira, T. Sato, T. Tsuda, and S. Fukao (1987), Characteristics of mesospheric internal gravity waves observed by MU radar, *Geophys. Res. Lett.*, *14*, 1154–1157, doi:10.1029/GL014i011p01154.

Nastrom, G. D. (1997), Doppler radar spectral width broadening due to beamwidth and wind shear, *Ann. Geophys.*, *15*, 786–796, doi:10.1007/s005850050497.

Nastrom, G. D., and F. D. Eaton (2006), Quasi-monochromatic inertia-gravity waves in the lower stratosphere from MST radar observations, *J. Geophys. Res.*, *111*, D19103, doi:10.1029/2006JD007335.

Nicolls, M. J., and C. J. Heinselman (2007), Three-dimensional measurements of traveling ionospheric disturbances with the Poker Flat Incoherent Scatter Radar, *Geophys. Res. Lett.*, *34*, L21104, doi:10.1029/2007GL031506.

Nicolls, M. J., C. J. Heinselman, E. A. Hope, S. Ranjan, M. C. Kelley, and J. D. Kelly (2007), Imaging of Polar mesosphere summer echoes with the 450-MHz Poker Flat Advanced Modular Incoherent Scatter Radar, *Geophys. Res. Lett.*, *34*, L20102, doi:10.1029/2007GL031476.

Nicolls, M. J., M. C. Kelley, R. H. Varney, and C. J. Heinselman (2009), Spectral observations of polar mesospheric summer echoes at 33 cm (450 MHz) with the Poker Flat Incoherent Scatter Radar, *J. Atmos. Sol. Terr. Phys.*, *71*, 662–674, doi:10.1016/j.jastp.2008.04.019.

Picone, J., A. Hedin, D. Drob, and A. Aikin (2002), NRLMSISE-00 empirical model of the atmosphere: Statistical comparisons and scientific issues, *J. Geophys. Res.*, *107*(A12), 1468, doi:10.1029/2002JA009430.

Raizada, S., M. P. Sulzer, C. A. Tepley, S. A. Gonzalez, and M. J. Nicolls (2008), Inferring *D* region parameters using improved incoherent scatter radar techniques at Arecibo, *J. Geophys. Res.*, *113*, A12302, doi:10.1029/2007JA012882.

Rietveld, M. T., and P. N. Collis (1993), Mesospheric observations with the EISCAT UHF radar during polar cap absorption events: 2. Spectral measurements, *Ann. Geophys.*, *11*, 797–808.

Riggin, D., D. C. Fritts, C. D. Fawcett, and E. Kudeki (1995), Observations of inertia-gravity wave motions in the stratosphere over Jicamarca, Peru, *Geophys. Res. Lett.*, *22*, 3239–3242, doi:10.1029/95GL03085.

Riggin, D. M., D. C. Fritts, C. D. Fawcett, E. Kudeki, and M. H. Hitchman (1997), Radar observations of gravity waves over Jicamarca, Peru during the CADRE campaign, *J. Geophys. Res.*, *102*, 26,263–26,282, doi:10.1029/96JD03675.

Rutledge, G. K., J. Alpert, and W. Ebuisaki (2006), NOMADS: A Climate and Weather Model Archive at the National Oceanic and Atmospheric Administration. [nomads.ncdc.noaa.gov], *Bull. Am. Meteorol. Soc.*, *87*, 327–341.

Sato, K. (1994), A statistical study of the structure, saturation and sources of inertio-gravity waves in the lower stratosphere observed with the MU radar, *J. Atmos. Terr. Phys.*, *56*, 755–774.

Serafimovich, A., P. Hoffmann, D. Peters, and V. Lehmann (2005), Investigation of inertia-gravity waves in the upper troposphere/lower stratosphere over Northern Germany observed with collocated VHF/UHF radars, *Atmos. Chem. Phys.*, *5*, 295–310.

Sloss, P. W., and D. Atlas (1968), Wind shear and reflectivity gradient effects on Doppler radar spectra, *J. Atmos. Sci.*, *25*, 1080–1089.

Smith, S. A., D. C. Fritts, and T. E. VanZandt (1987), Evidence for a saturated spectrum of atmospheric gravity waves, *J. Atmos. Sci.*, *44*, 1404–1410.

Strelnikova, I., M. Rapp, S. Raizada, and M. Sulzer (2007), Meteor smoke particle properties derived from Arecibo incoherent scatter radar observations, *Geophys. Res. Lett.*, *34*, L15815, doi:10.1029/2007GL030635.

Tepley, C. A., and J. D. Mathews (1978), Preliminary measurements of ion-neutral collision frequencies and mean temperatures in the Arecibo 80- to 100-km altitude region, *J. Geophys. Res.*, *83*, 3299–3302.

Tepley, C. A., J. D. Mathews, and S. Ganguly (1981), Incoherent scatter radar studies of mesospheric temperatures and collision frequencies at Arecibo, *J. Geophys. Res.*, *86*, 11,330–11,334.

Thomas, L., I. T. Prichard, and I. Astin (1992), Radar observations of an inertia-gravity wave in the troposphere and lower stratosphere, *Ann. Geophys.*, *10*, 690–697.

Thorne, A., U. Litzen, and S. Johansson (1999), *Spectrophysics: Principles and Applications*, Springer, Berlin.

Tsuda, T., Y. Murayama, H. Wiryosumarto, S. W. B. Harijono, and S. Kato (1994), Radiosonde observations of equatorial atmosphere dynamics over Indonesia: 2. Characteristics of gravity waves, *J. Geophys. Res.*, *99*, 10,507–10,516.

Turunen, E. (1996), Incoherent-scatter radar contributions to high-latitude *d*-region aeronomy, *J. Atmos. Terr. Phys*, *58*, 707–725.

Vadas, S. L., and D. C. Fritts (2001), Gravity wave radiation and mean responses to local body forces in the atmosphere, *J. Atmos. Sci.*, *58*, 2249–2279.

Vadas, S. L., and D. C. Fritts (2005), Thermospheric responses to gravity waves: Influences of increasing viscosity and thermal diffusivity, *J. Geophys. Res.*, *110*, D15103, doi:10.1029/2004JD005574.

Vadas, S. L., and M. J. Nicolls (2008), Using PFISR measurements and gravity wave dissipative theory to determine the neutral, background thermospheric winds, *Geophys. Res. Lett.*, *35*, L02105, doi:10.1029/2007GL031522.

Vadas, S. L., and M. J. Nicolls (2009), Temporal evolution of neutral, thermospheric winds and plasma response using PFISR measurements of gravity waves, *J. Atmos. Sol. Terr. Phys.*, *71*, 744–770, doi:10.1016/j.jastp.2009.01.011.

Vadas, S. L., D. C. Fritts, and M. J. Alexander (2003), Mechanism for the generation of secondary waves in wave breaking regions, *J. Atmos. Sci.*, *60*, 194–214.

Vincent, R. A., and M. J. Alexander (2000), Gravity waves in the tropical lower stratosphere: An observational study of seasonal and interannual variability, *J. Geophys. Res.*, *105*, 17,971–17,982, doi:10.1029/2000JD900196.

Walterscheid, R. L. (1981), Inertio-gravity wave induced accelerations of mean flow having an imposed periodic component - Implications for tidal observations in the meteor region, *J. Geophys. Res.*, *86*, 9698–9706.

Walterscheid, R. L., G. G. Sivjee, G. Schubert, and R. M. Hamwey (1986), Large-amplitude semidiurnal temperature variations in the polar mesopause - Evidence of a pseudotide, *Nature*, *324*, 347–349.

Weinstock, J. (1981), Energy dissipation rates of turbulence in the stable free atmosphere, *J. Atmos. Sci*, *38*, 880–883.

Williams, B. P., D. C. Fritts, L. Wang, C. Y. She, J. D. Vance, F. J. Schmidlin, R. A. Goldberg, A. Müllemann, and F.-J. Lübken (2004), Gravity waves in the arctic mesosphere during the MaCWAVE/MIDAS summer rocket program, *Geophys. Res. Lett.*, *31*, L24S05, doi:10.1029/2004GL020049.

Zhu, X., and J. R. Holton (1987), Mean fields induced by local gravity-wave forcing in the middle atmosphere, *J. Atmos. Sci.*, *44*, 620–630.

R. B. Cosgrove, C. J. Heinselman, and M. J. Nicolls, Center for Geospace Studies, SRI International, 333 Ravenswood Avenue, Menlo Park, CA 94025, USA. (michael.nicolls@sri.com)

M. C. Kelley and R. H. Varney, School of Electrical and Computer Engineering, Cornell University, Ithaca, NY 14953, USA.

P. A. Stamus and S. L. Vadas, CoRA Division, Northwest Research Associates, Boulder, CO 80301, USA.